Beam dynamical behaviour of the MESA SRF structures under recirculating operation

Dissertation
zur Erlangung des Grades
"Doktor der Naturwissenschaften"
am Fachbereich Physik, Mathematik und Informatik
der Johannes Gutenberg-Universität
in Mainz

Christian Philipp Stoll M.Sc.
geb. am 07.05.1990 in Speyer

Mainz, den 13. Mai 2020

Datum der mündlichen Prüfung: 01.10.2020

Christian Philipp Stoll
Institut für Kernphysik
Johann-Joachim-Becher-Weg 45
Johannes Gutenberg-Universität
D-55099 Mainz
stollc@uni-mainz.de

Abstract

Energy Recovery Linacs (ERLs) are a novel type of electron accelerators which circumvent certain problems with beam quality that arise in circular machines, while also limiting the amount of power needed for acceleration compared to linear accelerators (Linacs). The idea was first proposed by M. Tigner in [1]. In an ERL machine, the electrons are fed from the source into the accelerating cavities and are then used for example in minimally invasive nuclear physics experiments [2] or to drive a radiation source [3]. After the experimental use, the electrons are recirculated back into the cavities with a phase shift of 180° with respect to the accelerating field. This allows the particles to be decelerated in the cavities' electric field and to feed their kinetic energy back into the cavities. The Mainz Energy-recovering Superconducting Accelerator (MESA) is currently under construction at Johannes Gutenberg University Mainz. For MESA stage 1 operation, a beam current of 1 mA will be accelerated four times in two cryomodules up to an energy of 105 MeV. 100 MeV of beam energy can be recovered, and the beam will be dumped at the injection energy of 5 MeV. This leads to a significantly reduced power demand from the wall but requires superconducting cavities operated at 1.8 K with high quality factors to maintain the accelerating field in the cavities. For MESA, stage 2 operation with up to 10 mA is planned. High-current beams pose significant challenges to beam dynamics, due to, for example, space charge at low energies and transverse Beam Break Up (BBU) caused by dipole Higher Order Modes (HOMs) in the superconducting cavities. The measurement of HOMs in the MESA cavities performed at Helmholtz-Institut Mainz (HIM), their impact on beam dynamics, and the limits of achievable beam currents imposed by BBU are presented in this work.

Zusammenfassung

Energie rückgewinnende Linearbeschleuniger (ERL) sind ein neuartiger Beschleunigertyp, der die Strahlqualitätseinschränkungen von Zirkularbeschleunigern umgeht, aber gleichzeitig den Leistungsaufwand zur Beschleunigung im Vergleich zu Linearbeschleunigern reduziert. Die Idee wurde zuerst von M. Tigner vorgeschlagen [1]. In einem ERL werden die Elektronen von der Quelle in die Beschleunigungsstrukturen geleitet und dann für z.B. minimalinvasive Teilchenphysik-Experimente [2] oder zur Erzeugung brillianter Strahlung genutzt [3]. Nach der Interaktion mit dem Experiment werden die Elektronen erneut mit einem Phasenvorschub von 180° in die Beschleunigungsstrukturen geleitet. Die Teilchen werden dadurch abgebremst und ihre kinetische Energie wird an das elektromagnetische Feld der Beschleunigerstrukturen zurückgegeben. Der Mainz Energy-recovering Superconducting Accelerator (MESA) wird zurzeit an der Johannes Gutenberg-Universität aufgebaut. Für Phase 1 von MESA wird ein Strahlstrom von 1 mA viermal in zwei Kryomodulen bis auf eine Energie von 105 MeV beschleunigt. 100 MeV der Strahlenergie können zurückgewonnen werden und der Strahl wird bei 5 MeV gestoppt. Dies führt zu einer signifikanten Einsparung von Anschlussleistung, benötigt aber supraleitende Beschleunigungsstrukturen, die bei 1,8 K betrieben werden und hohe Güten aufweisen müssen, um die zur Beschleunigung notwendigen Feldstärken aufrecht zu erhalten. Für die zweite Phase von MESA ist Strahlbetrieb mit bis zu 10 mA vorgesehen. Elektronenstrahlen mit hohem Strahlstrom stellen spezielle Anforderungen an die Strahldynamik, unter anderem durch Raumladung bei niedrigen Strahlenergien und durch das so genannte Beam Break Up (BBU), welches durch Dipol-Moden höherer Ordnung (Higher Order Modes (HOMs)) in den Beschleunigungsstrukturen ausgelöst wird. Die Messung der Moden höherer Ordnung, die am Helmholtz-Institut Mainz

(HIM) durchgeführt wurde, ihr Einfluss auf die Strahldynamik und die Beschränkungen des maximalen Strahlstroms durch BBU werden in dieser Arbeit vorgestellt.

Contents

1 Introduction

Particle accelerators are an important tool in the research of fundamental processes. Their main task is to provide a stable beam of particles for various applications, e.g. light sources, nuclear and particle physics experiments or production of exotic matter. For the research of effects which could hint at physics beyond the standard model, very high precision, high average current in continuous wave (CW) operation, and very stable beam conditions are necessary. This is the goal of the electron accelerator MESA and the accompanying experiments. To provide these high currents in CW operation, a lot of Radio Frequency (RF) power is required to accelerate the particles. A new concept in electron accelerators, the so-called Energy Recovery Linac (ERL), bypasses this problem by reusing beams that were used in minimally invasive experiments, decelerating them in the accelerating cavities and thus feeding the beam energy back to the RF fields. A fundamental limit to the maximum achievable beam current of electron accelerators is the interaction of the beam with unwanted Higher Order Modes (HOMs) in the accelerating cavities, which can lead to the Beam Break Up (BBU) instability. BBU occurs when the electrons in the accelerator form a positive feedback loop with a HOM of the accelerating cavities and the feedback gain of the HOM is larger than the decay of the HOM. Therefore, superconducting cavities are more prone to be affected due to their high quality factors, which lead to long lifetimes of excited HOMs. Energy from electrons that travel off axis is fed into the HOM, and subsequent electron bunches are deflected by the magnetic field of the HOM. When deflected bunches enter the cavity again, as is the case in recirculating machines or ERLs, they can have a larger transverse offset, feeding more energy to the HOM. A feedback loop can arise, which can lead to total loss of the beam, thereby limiting the maximum beam current that can be accelerated in the machine. The maximum

achievable beam current before BBU occurs is called threshold current. For the MESA project, superconducting (SC) cavities of the TESLA/XFEL type are used. During the manufacturing of these cavities and as part of the Site Acceptance Test (SAT), the HOM spectra of the MESA cavities were measured in two different setups. This allows for the investigation of property changes due to manufacturing as well as predictions of the achieved manufacturing tolerances. By considering simulation data available for the TESLA cavities, a model of the accelerators with emphasis on the BBU instability was created. Beam dynamics studies performed with simulated cavity parameters were compared to studies performed with the measurement data. With the help of the simulation data, even effects due to modes not easily measurable in the real cavity were investigated.

In the next chapter, MESA and the accompanying experiments are presented. Chapter 3 gives a short introduction to the basic concepts of electron acceleration and transport. The concept of superconducting radio-frequency cavities is introduced in chapter 4. Also the figures of merit for the simulation of threshold currents are explained. The fundamental theory of BBU as well as the application to ERLs is presented in chapter 5. The results and methodology of the measurements of the cavity HOM parameters and the simulation of threshold currents are presented in chapter 6. A short outlook is given on the topic of HOM coupler heating followed by a conclusion and a general outlook.

2 MESA

The Mainz Energy-recovering Superconducting Accelerator (MESA) is a small-scale, multi-turn, double-sided, recirculating Linear accelerator (Linac) with vertical stacking of the return arcs currently under construction at the Johannes Gutenberg University Mainz [4]. As civil construction of the new accelerator hall progresses, part of the machine can be installed in already existing parts of the building. The layout of the facility and the physics program planned are presented in this chapter.

2.1 Layout of the MESA Facility

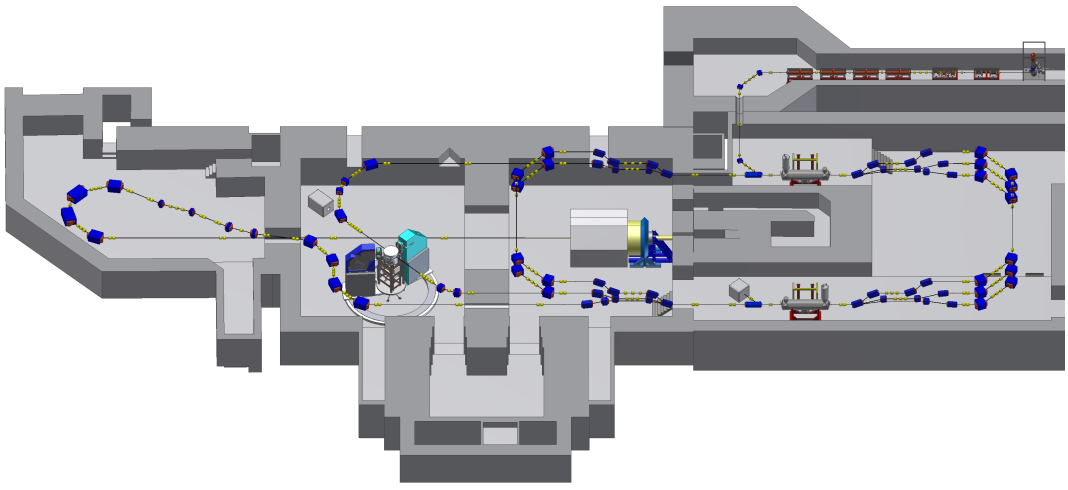

Figure 2.1: Layout of the MESA facility. Here the electron source and the injector Linac will be built and commissioned in an already existing Linac tunnel, while civil construction continues in the experimental halls.

The layout of the MESA facility is shown in Fig. 2.1. It includes the possibility to set up the electron source and injector Linac in an already existing part of the building even while civil construction continues in the main experimental halls. In this layout, the beam direction through the cavities is inverted as compared to the previous set-up which is discussed in this work.

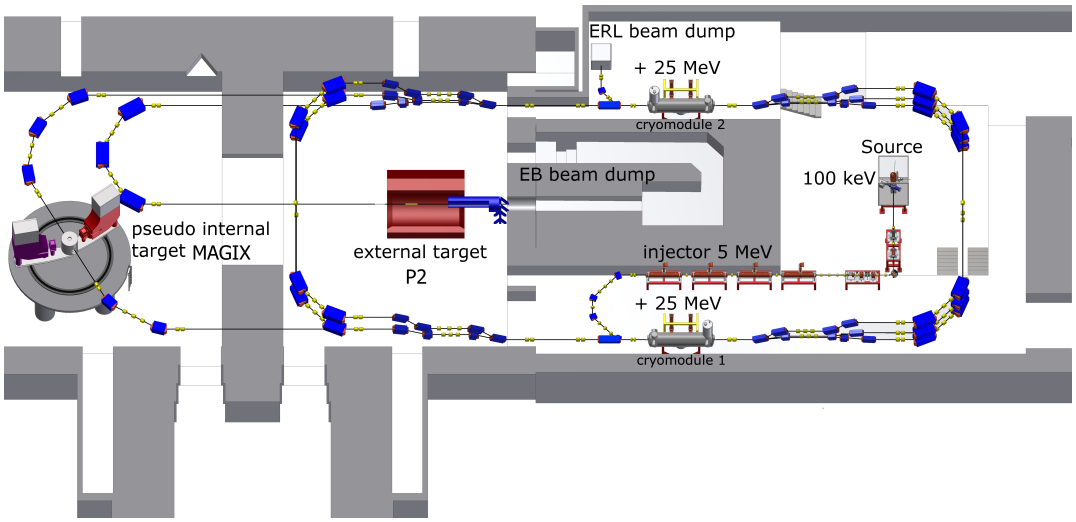

Figure 2.2: Past layout of the MESA facilities as it was used for the calculations presented in this work. The electron source is positioned behind the beam dump of the external beam and the beam circulates through the accelerator counterclockwise.

MESA will be a multi-purpose user facility for nuclear and particle physics experiments. The physics experiments which are planned will be presented in the next section. The beam is generated by a 100 keV polarized DC electron source called STEAM (Small Thermalized Electron Source at Mainz) [5], which uses a Gallium Arsenide photo cathode irradiated by a pulsed laser. The source is followed by a low energy beam transport system including a double Wien filter setup for spin manipulation, a chopper and a buncher system [6]. The buncher system operates one cavity at the fundamental 1.3 GHz and another cavity at the second harmonic of 2.6 GHz for longitudinal bunch compression. This low-energy beam transport system provides up to 1 mA in continuous wave (CW) operation with a bunch charge of up to 0.77 pC and a polarisation of up to 85 %. The low-energy beam transport system is followed by the normal-conducting injector Linac, the so-called Milliampere Booster (MAMBO) [7]. It consists of four cavities and provides 5 MeV of energy gain. The beam is then injected through a flexible momentum compaction (FMC) arc [8] into the first

superconducting cryomodule. The cryomodules are produced by industry and are of a modified ELBE type [9], each containing two TESLA/XFEL type [10], 9-cell cavities operated at 1.3 GHz. They are supposed to deliver 12.5 MV m^{-1} of accelerating gradient with a Q_0 of 1.25×10^{10}. After the cryomodule, a vertical beam splitter section is able to accept 3 different energies: 30, 80, and 130 MeV, which are then delivered to the vertically stacked arcs. The beam with the highest energy is bent into the bottom beam line because of its higher rigidity. In a vertical merger section, the beams are recombined and accelerated a second time in the second cryomodule. By means of a second vertical beam splitter, the beams with energies of 55 MeV, 105 MeV, or 155 MeV are either recirculated or fed to the experimental areas, depending on which mode of operation is chosen. MESA will be able to run in two different modes, one being a thrice-recirculating external beam (EB) mode with up to 155 MeV and 150 µA of beam current where the full-energy beam is dumped after being used at the P2 experiment [11]. The other is a twice-accelerating and also twice-decelerating four-pass energy recovery (ER) mode with up to 1 mA of beam current at a maximum energy of 105 MeV. Due to the nature of the energy recovery process on the decelerating passes, which means injecting the beam into the cryomodules a second time with a phase shift of 180°, allowing the electrons to be decelerated and thus returning some of their kinetic energy to the electromagnetic field inside the cavity, the beam is dumped at an energy of 5 MeV. While the power fed to the cavities in EB mode amounts to 22.5 kW, it is zero in ER mode assuming an energy recovery efficiency of 100 %, even though the current is more then 6 times larger. This advantage allows to perform nuclear and particle physics experiments at very high luminosities as it is described in the next section.

2.2 Nuclear Physics Experiments at MESA

The main purpose of MESA is to provide high-brilliance CW electron beams with very stable conditions for two planned nuclear physics experiments. The P2 experiment [11], which runs in an external beam mode with 150 µA of beam current, performs a high-precision measurement of the weak mixing angle, the

so-called Weinberg angle $\sin^2\theta_w$ from the measurement of parity violation (PV) in elastic electron-proton scattering. The expected size of the parity-violating asymmetry is $A_{PV} \approx 30$ ppb (parts per billion); the P2 experiment aims for a total uncertainty of $\Delta A_{PV} \approx 0.5$ ppb, which places high demands on the accelerator concerning beam stability and on the experiment. A 60 cm long liquid hydrogen target together with a beam current of 150 µA will provide a luminosity of $\mathcal{L} \approx 2.4 \times 10^{39}\,\mathrm{s^{-1}\,cm^{-2}}$. The 155 MeV beam is then dumped in the EB beam dump as can be seen in Fig. 2.2. A solenoid spectrometer with fused silica detectors will be set up for the detection of the scattered electrons and the separation of background events. A tracking system based on High Voltage Monolithic Active Pixel Sensors (HV-MAPS) will be installed in order to determine the momentum transfer Q^2 with high precision. Two types of electron polarimeters are under development, a so-called Hydro Møller polarimeter [12] and a Double Scattering Mott Polarimeter (DSP) [13]. The goal is to determine the degree of polarization of the electron beam with an accuracy of $\Delta P/P = 0.5\,\%$.

A parasitic experiment will be integrated into the facility, running in parallel with the P2 experiment, trying to detect rare particles that might be created in the beam dump, which is called beam dump experiment (BDX) [14].

The MesA Gas Internal target eXperiment MAGIX [2], see Fig. 2.2 on the left, is designed with a windowless gas jet target to conduct nuclear and particle physics experiments on different gases ranging from hydrogen up to xenon. It gives ample opportunity to investigate for example the proton radius and to search for particles beyond the standard model. Different challenges arise from this sort of low-impact target experiment. Since it will be a windowless target, scattering effects in the area around the experiment, with notably worse vacuum conditions than in the rest of the accelerator, as well as scattering of the beam itself with the gas jet target have to be considered carefully. The experiment itself requires an energy spread of $\approx 5 \times 10^{-4}$ and a focussed beam on the target. The beam target interaction should be kept to a minimum to allow for energy recovery. Special emphasis is put on the beam-induced halo and how it transfers through the machine in ER mode [15]. The stage 1 beam of 1 mA and an energy of 105 MeV will produce a luminosity $\mathcal{L}$ in the order of $10^{35}\,\mathrm{s^{-1}\,cm^{-2}}$,

and at a later stage an upgrade to 10 mA is planned to further increase the luminosity. Investigation of the cavities' behaviour while being exposed to such high currents is mandatory to ramp up the intensity and to maintain the beam quality. To give an overview of some of the theoretical concepts used in this work, the following chapter describes the theory of electron acceleration and transport.

3 Fundamentals of Particle Acceleration and Transport

In this chapter the principle of acceleration of charged particles will be motivated and the mathematical modelling of accelerator machines will be presented. The study of beam dynamics for accelerators grew ever more complex over the last decades by the aim to go to higher currents, higher energies and higher brightness. Therefore, careful consideration of effects previously not deemed detrimental to accelerator performance is necessary.

3.1 Basic Principle of Electron Acceleration

Electrons and charged particles in general are accelerated by Radio Frequency (RF) fields. By having a so-called cavity, that is a structure that houses oscillating RF fields of the frequency used for acceleration, electrons have to be injected at the right time to meet the accelerating crest of the RF wave as illustrated in Fig. 3.1. This implies certain conditions on the movement of the particles in the RF fields. For example, to achieve continuous acceleration, the particle has to travel a distance equal to half the wavelength of the accelerating RF field's frequency (assuming particles travelling at the speed of light). The electric field configuration inside a 9-cell cavity operated in π mode is shown in Fig. 3.2. As can be seen, while one cell has an accelerating field, its neighbour contains a field in which the phase is advanced by 180° (π). If the particle is not travelling at the speed of light, its phase with respect to the crest of the accelerating phase will change during the acceleration process, resulting in less

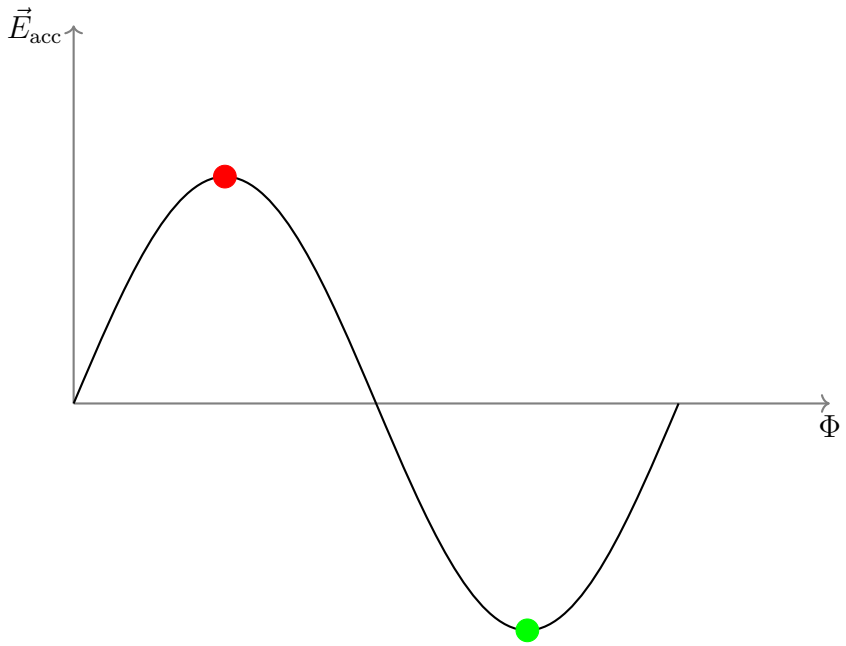

Figure 3.1: Illustration of the basic principle of RF acceleration. For acceleration, a particle (red dot) has to arrive on crest to gain the maximum possible energy. Energy is transferred from the RF field to the particle. For deceleration, a particle (green dot) has to arrive at the trough to give its energy back to the RF field.

energy gain for particles with $v < c$. For MESA this phase slippage effect needs to be considered in the first cryomodule pass (5 MeV to 30 MeV) only.

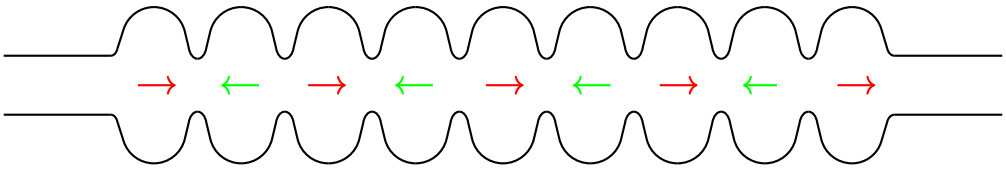

Figure 3.2: Simplified electric field configuration of the π accelerating mode inside a TESLA cavity. The colors indicate the same situation as in Fig. 3.1, where a red arrow indicates an accelerating electric field and a green arrow indicates a decelerating electric field. The phase difference between neighbouring cells is $180° = \pi$.

3.2 Basics of Electron Transport

The trajectory of particles can be controlled by external electric and magnetic fields. The Lorentz force is given by:

$$F_L = q(\vec{E} + \vec{v} \times \vec{B}), \tag{3.1}$$

where q is the electric charge of the particle, $\vec{E}$ and $\vec{B}$ are the external electric and magnetic fields respectively and $\vec{v}$ is the velocity of the particle. It is evident that in order to change the trajectory of a particle, it is convenient to apply magnetic fields, and to accelerate the particles, electric fields are used in the form of the aforementioned RF fields. Since the magnetic force is always perpendicular to the velocity, it cannot change the energy of the particles. Thus, in accelerators, dipole magnets are used for the deflection of charged particles, quadrupole magnets are used for the focussing of particle bunches consisting of multiple particles, and RF accelerating cavities are used for acceleration.

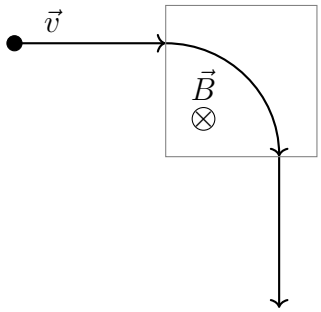

Figure 3.3: Deflection of a particle carrying a negative charge in the homogeneous field of a dipole magnet. The direction of the magnetic field points inside the paper and is only active inside the rectangular area.

For the lossless transport of charged particles, ultra-high vacuum conditions are also required, since collisions with residual gas particles can deteriorate the beam quality significantly.

3.3 Mathematical Model of Beam Dynamics

This section follows the description of beam dynamics as presented in section 2.2.1 in [16]. In accelerator physics, a co-moving coordinate frame is used to simplify the process of describing bent trajectories as a deviation from reference orbit.

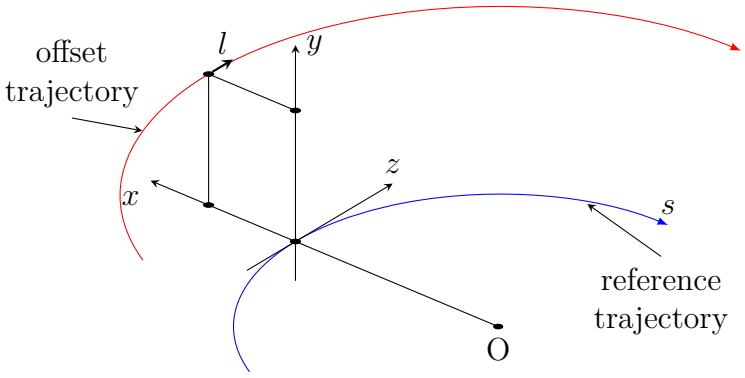

Figure 3.4: Sketch of the variables used for the description of a co-moving coordinate frame.

The coordinate s follows the reference trajectory. The plane perpendicular to the direction of travel is spanned by two orthogonal vectors $\vec{x}$ for the horizontal plane and $\vec{y}$ for the vertical plane, describing the displacement of a trajectory with respect to the reference trajectory, as shown in Fig. 3.4. x' and y' are used to describe the angular deviation in the x-y plane:

$$x' = \frac{\mathrm{d}p_x}{\mathrm{d}p_z} = \frac{\mathrm{d}x}{\mathrm{d}s}, \quad y' = \frac{\mathrm{d}p_y}{\mathrm{d}p_z} = \frac{\mathrm{d}y}{\mathrm{d}s}.$$

This is possible due to the fact that the longitudinal momentum in beam direction is much larger than the transverse momenta; this is called the paraxial approximation. Transverse momenta can then be replaced by transverse angles usually in the order of mrad, which then replace the canonic coordinates. For a full description of a particle, the coordinate l is needed as the longitudinal offset of the particle from the reference trajectory as well as $\frac{\Delta p}{p_0}$, the momentum deviation of the particle with respect to the reference momentum. It is convenient to describe l in units of time deviation to the reference particles when ultra-relativistic beams are described, or in phase deviation with respect to the accelerating frequency. A particle can then be described by a vector $\vec{X}$:

$$\vec{X}^{\intercal} = \left(x, x', y, y', l, \frac{\Delta p}{p_0}\right) \tag{3.2}$$

The transformation of a vector $X(0)$ at position 0 to another position $X(s)$ along the central trajectory is described by:

$$\mathbf{X}(s) = \mathbf{R}\mathbf{X}(0), \tag{3.3}$$

where $\mathbf{R}$ is a 6×6 matrix. All linear physics is contained in $\mathbf{R}$ representing each type of magnet, accelerating structure, drift, etc. and is derived from the equations of motion of a particle travelling through static magnetic fields. Equation 3.3 can be expanded as:

$$\mathbf{R}\mathbf{X}(0) = \begin{pmatrix} R_{11} & R_{12} & R_{13} & R_{14} & 0 & R_{16} \\ R_{21} & R_{22} & R_{23} & R_{24} & 0 & R_{26} \\ R_{31} & R_{32} & R_{33} & R_{34} & 0 & R_{36} \\ R_{41} & R_{42} & R_{43} & R_{44} & 0 & R_{46} \\ R_{51} & R_{52} & R_{53} & R_{54} & 1 & R_{56} \\ 0 & 0 & 0 & 0 & 0 & 1 \end{pmatrix} \begin{pmatrix} x \\ x' \\ y \\ y' \\ l \\ \Delta p/p_0 \end{pmatrix}.$$

For static magnetic fields, p_0 and $\Delta p/p_0$ are constants of motion, which results in the 0 elements in row 6. The 0 elements in column 5 are a result of the independence of $x, x', y, y', \Delta p/p_0$ on l. If all magnets in the system have midplane symmetry, and assuming only horizontally deflecting dipole magnets, then in first order optics the x- and y-motions decouple and:

$$\mathbf{R} = \begin{pmatrix} R_{11} & R_{12} & 0 & 0 & 0 & R_{16} \\ R_{21} & R_{22} & 0 & 0 & 0 & R_{26} \\ 0 & 0 & R_{33} & R_{34} & 0 & 0 \\ 0 & 0 & R_{43} & R_{44} & 0 & 0 \\ R_{51} & R_{52} & 0 & 0 & 1 & R_{56} \\ 0 & 0 & 0 & 0 & 0 & 1 \end{pmatrix}.$$

Multiplying single element matrices with one another yields the description of a beamline of multiple elements by a single **R** matrix:

$$\mathbf{R}(s) = \mathbf{R}(n) \cdots \mathbf{R}(i) \cdots \mathbf{R}(2)\mathbf{R}(1). \tag{3.4}$$

Some important beam matrix elements are for example:

$$R_{21} = \frac{-1}{f_x}, \quad R_{43} = \frac{-1}{f_y},$$

where f_x, f_y are the focal lengths of the system in their respective planes, describing the focussing strength of quadrupoles as well as other elements. R_{16} and R_{26} are the dispersion and the angular dispersion in the x plane and R_{56} is the so-called momentum compaction:

$$R_{56} = \int \frac{R_{16}(s)}{\rho(s)} \mathrm{d}s, \tag{3.5}$$

due to the presence of dispersion on curved trajectories. The **R** matrix allows the tracking of single particles through any system of optical elements. To track a bunch of particles through a given system, the beam is characterized by the so-called phase space ellipse. The equation of an ellipse in n-D can be given by the matrix equation:

$$\mathbf{X}^\intercal \Sigma^{-1} \mathbf{X} = 1 \tag{3.6}$$

For example, in 2-D:

$$\mathbf{X} = \begin{pmatrix} x \\ x' \end{pmatrix}, \quad \Sigma = \begin{pmatrix} \sigma_{11} & \sigma_{21} \\ \sigma_{21} & \sigma_{22} \end{pmatrix},$$

applying above equation to Eq. 3.6 yields:

$$\sigma_{22} x^2 - 2\sigma_{21} x x' + \sigma_{11} x'^2 = \det \Sigma. \tag{3.7}$$

This can be rewritten in the so-called Courant-Snyder notation:

$$\Sigma = \begin{pmatrix} \sigma_{11} & \sigma_{21} \\ \sigma_{21} & \sigma_{22} \end{pmatrix} = \epsilon \mathbf{T}, \quad \mathbf{T} \equiv \begin{pmatrix} \beta & -\alpha \\ -\alpha & \gamma \end{pmatrix},$$

with $\det \mathbf{T} = 1$. The equation of the ellipse (Courant-Snyder invariant) is then given by:

$$\mathbf{X}^\intercal \mathbf{T}^{-1} \mathbf{X} = \epsilon,$$

$$\gamma x^2 + 2\alpha x x' + \beta x'^2 = \epsilon, \tag{3.8}$$

where α, β, γ are the Courant-Snyder or Twiss parameters. The area of the ellipse is $A = \pi\epsilon$. The quantity ϵ is known as the emittance of the beam and can be seen as a measure of the beam quality.

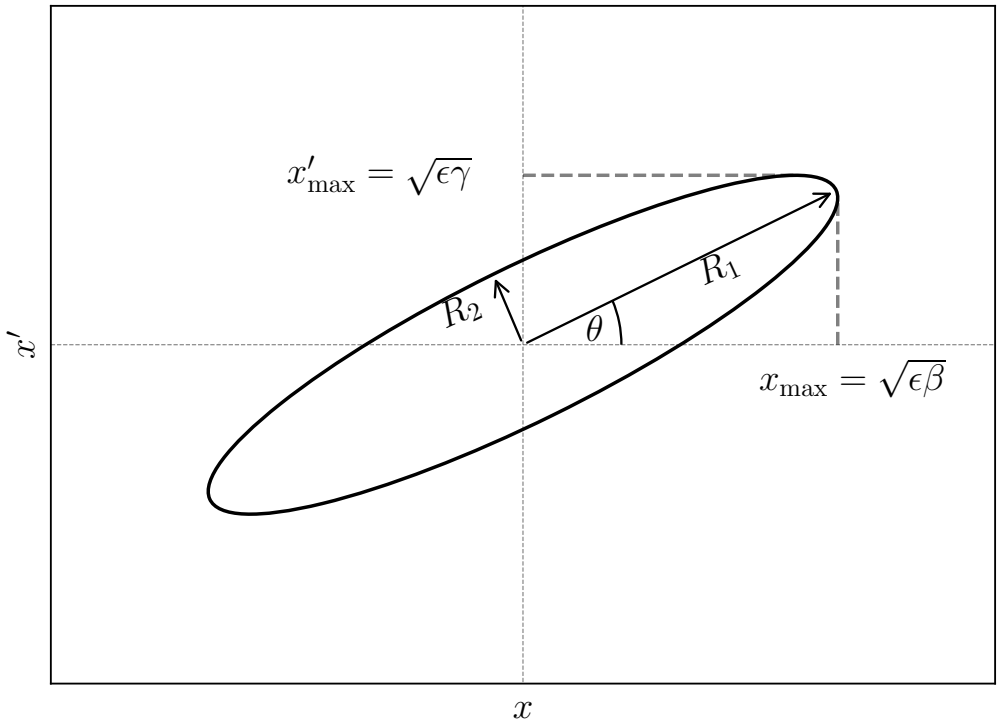

Figure 3.5: Sketch of the parameters used to describe phase space ellipses in terms of the Twiss parameters. The size of the ellipse is fully described by the emmittance and the Twiss parameters.

Some useful parameters of phase space ellipses that can later be used for fitting results of particle tracking simulations are listed below:

$$\gamma = \frac{(1+\alpha^2)}{\beta}, \quad H = (\beta + \gamma)/2,$$

$$R_1 = \sqrt{1/2}(\sqrt{H+1} + \sqrt{H-1}),$$

$$R_2 = \sqrt{1/2}(\sqrt{H+1} - \sqrt{H-1}).$$

$$\theta = \frac{1}{2}\arctan\left(\frac{2\alpha}{\gamma - \beta}\right),$$

where θ is the angle the half axis R_1 makes with the positive x-axis.

3.4 Accelerator Tracking Codes

For complex accelerators containing several hundred optical elements, it is convenient to use dedicated simulation or tracking codes that reduce the amount of work that has to be done to compute an R-matrix or to automatically perform the matching of different sections of the accelerator. In this work, the two main codes used are MAD-X (Methodical Accelerator Design) [17, 18] and ELEGANT (ELEctron GEneration ANd Tracking) [19, 20]. Both codes are capable of full 6-D tracking of particles. Since the MESA lattice was optimized mainly using the optimisation routines available in MAD-X, it was also chosen as a starting point for this work. One major shortcoming of MAD-X is the complicated implementation of RF cavities. In ELEGANT, the implementation of RF cavities is as simple as including magnets, and even different cavity edge focussing effects are considered, the importance of which will be discussed later.

3.4.1 Beam Optics Matching

A typical problem in the design stage of an accelerator is matching. At MESA, the MAGIX experiment requires certain beam parameters at the interaction point, a small beam spot size $< 250\,\mu\text{m}$ (can be achieved through focussing magnets before the interaction point) and a low energy spread (has to be optimised along the full accelerator and is ultimately limited by the source and injector performance). To achieve these design values at a certain point in the accelerator, it is not only necessary to carefully optimise the arc optics, it also has to be made sure that each part is matched to subsequent parts so that

no phase space deterioration occurs. For this work, the interesting interaction occurs in the superconducting RF cavities used for the main acceleration. It is expected that the lowest energy beam (5 MeV) is most susceptible since its beam rigidity is the lowest among all beams present in MESA. Simulations for the MESA low energy beam transport apparatus (MELBA) [6] have already been performed by C. Matejcek and R. Heine [21]. To inject the electrons from the injector Linac into the main Linac, an injection arc is necessary. This arc was designed and matched to the first cryomodule as part of this work.

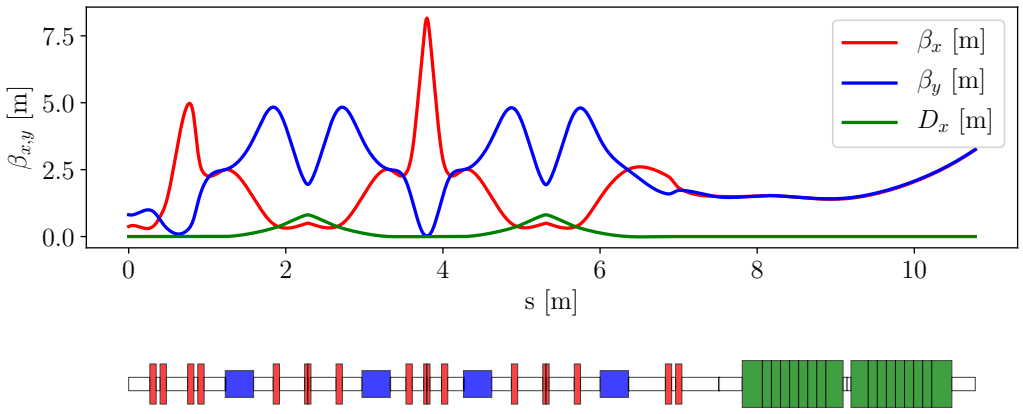

Figure 3.6: Optimised result for the injection arc optics. The red and blue lines are the β functions in the horizontal and vertical dimension along the beamline. The green curve is the horizontal dispersion. Red squares mark positions of quadrupole magnets, blue squares are dipole magnets, and green squares depict RF cavity cells.

The beam optics layout of the injection arc is shown in Fig. 3.6. With the help of four quadrupole magnets at the beginning of the arc, a high acceptance of the injection arc is achieved. Four dipole magnets (at the position of the blue squares) are necessary to achieve the 180° bending necessary to connect to the main Linac. To obtain some flexibility in the value of R_{56}, a total of nine quadrupole magnets are used between the dipoles. The goal of the matching was to achieve the design β functions after the cryomodule, matching the design parameters for the subsequent MESA arc 1. Since the arcs were designed with the goal of β functions before and after cryomodules of the order of the active length of the cryomodule to suppress BBU ($\beta_{x,y} = 3.2646\,\mathrm{m}$ and $\alpha = -1$) these parameters had to be achieved by manipulation of the optics before the cryomodule. The β function at a certain point determines

the transverse beam dimensions at that position as can be seen in Fig. 3.5, $x_{\max} = \sqrt{\epsilon\beta}$. The horizontal and vertical β functions along the beamline give an impression of the beam dimensions at every position. Inside the accelerating cavities a round beam ($\beta_x = \beta_y$) with zero dispersion ($D_{x,y} = 0$) is optimal. Cavity edge focussing was considered in these simulations. Another goal of this optimisation was to find the possibility of flexible momentum compaction R_{56}. If this parameter is adjustable, the injection arc can be used as a bunch compressor, further improving the quality of the beam at the location of the experiment. The basic idea of bunch compressing is that we imprint a so-called momentum chirp on the bunch by off-crest acceleration in the injector Linac MAMBO, which leads to a correlation of momentum and the longitudinal position of electrons in the bunch. The R_{56} element describes the dependence of longitudinal beam position on momentum. By applying a certain amount of R_{56}, particles in the bunch are rearranged according to their momentum. Therefore, the beam can be rotated in longitudinal phase space and the bunch can be compressed at the position of the first superconducting cavity.

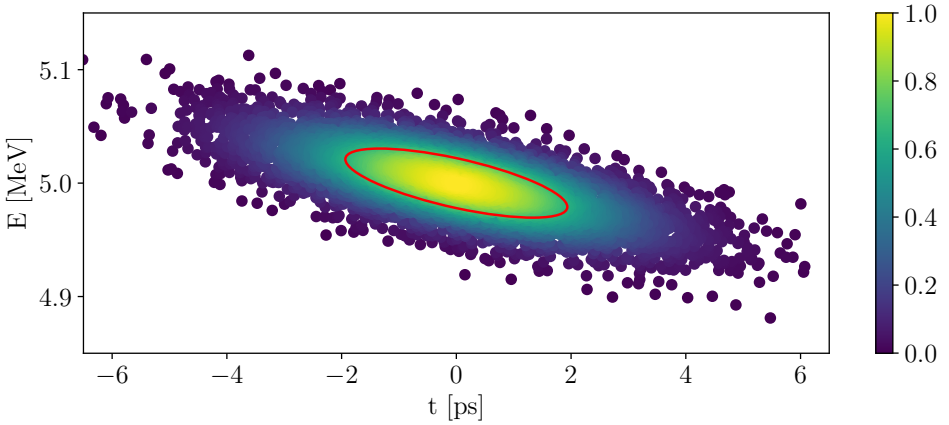

Figure 3.7: Longitudinal phase space with a momentum chirp of −6.6 % as could be produced by the MAMBO injector. The red ellipse denotes the 1σ distribution of the bunch.

In Fig. 3.7 the initial longitudinal phase space with a momentum chirp is shown. There is a clear dependence of momentum on longitudinal position in the bunch, described here as time offset to the reference particle. This bunch was then tracked through the injection arc, with $R_{56} = 0.15\,\mathrm{m}$ for the full arc. The

resulting longitudinal phase space after tracking through the arc operated as a bunch compressor is shown in Fig. 3.8.

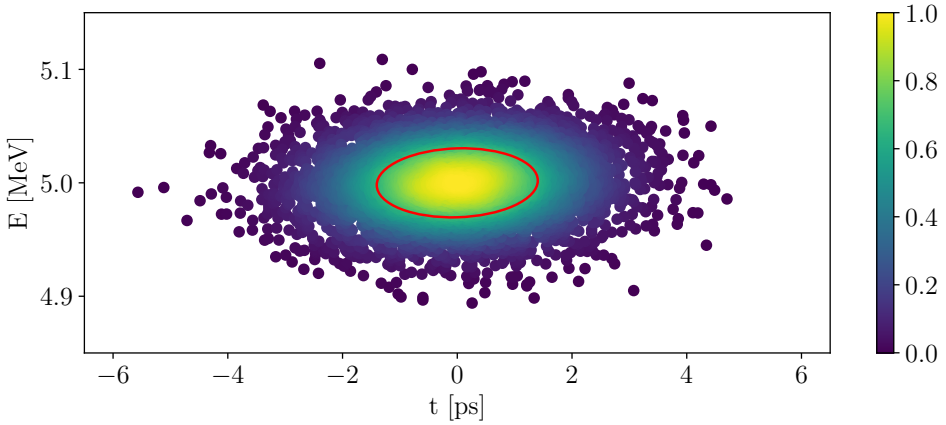

Figure 3.8: Longitudinal phase space after travelling through the injection arc operated as a bunch compressor. The bunch was longitudinally compressed. The red ellipse denotes the 1σ distribution of the bunch.

It is shown in Ref. [22] that the injection arc can be matched to the cryomodule in the presence of space charge for 10 mA of beam current with corrections of up to 15 % in quadrupole gradients.

3.4.2 Particle Tracking

With the use of accelerator codes, it is possible to observe the effects of single particle interactions. The cost of computation scales with the number of particles and is especially time-consuming for a large number of particles (10^6 to 10^9) and if inter-particle interactions are considered (e.g. space charge). Particle tracking allows to investigate real beam distributions in 6-D as for example provided by the injector and how they change along the beamline. Since no cavities could be implemented in MAD-X, the investigation of particle distributions was done using ELEGANT. A nice application of tracking is the investigation of the influence of deviations of element positions or magnet strengths on beam quality to give an estimate of how robust the lattice is and with which accuracy the real machine has to be aligned. A perfectly aligned machine with no deviations only exists as a mathematical model, but results

from misalignment studies can easily be compared with alignment accuracies realised at other facilities.

4 Superconducting Radio Frequency Cavities

Superconducting radio frequency (SRF) cavities are an essential tool for small-scale, high-energy accelerators. They are especially efficient when high beam currents >500 µA are used in an energy recovery scheme. Compared to their normal-conducting counterparts, they are able to reach and maintain a much higher electric field strength in CW operation—up to $30\,\mathrm{MV\,m^{-1}}$ have been shown with SRF cavities [23]—while gradients in the order of $15\,\mathrm{MV\,m^{-1}}$ are readily achievable with current technology. The E-XFEL uses SC cavities of the TESLA type, is operated in pulsed mode and uses a field of $23\,\mathrm{MV\,m^{-1}}$. At LCLSII an accelerating field of $16\,\mathrm{MV\,m^{-1}}$ in CW operation is planned [24]. Normal conducting radio frequency (NRF) cavities usually reach a field of up to $1\,\mathrm{MV\,m^{-1}}$ in CW operation, but can reach up to $100\,\mathrm{MV\,m^{-1}}$ in pulsed operation with a low duty cycle. For example, the CW electron accelerator MAMI [25] uses NRF cavities with gradients of about $1\,\mathrm{MV\,m^{-1}}$; the problem here is that the power losses to the cavity walls, which have to be actively cooled, are in the order of $15\,\mathrm{kW\,m^{-1}}$. While the SRF technology brings the benefit of higher gradients and smaller footprint of the accelerator facility, there are certain obstacles, such as the required cryogenic infrastructure [26] to make the SRF cavities work as well as more stringent requirements on beam losses, vacuum conditions and overall operational safety. Energy recovery has been shown at the Novosibirsk FEL facility [27] for normal conducting cavities, with low energy (several MeV) but high current (30 mA) in CW operation. Due to their higher quality factors, there is an inherent advantage in SRF cavities for energy recovery operation as the maximum ER efficiency can be very close to 100 %. For MESA, four TESLA-type cavities housed in two modified

ELBE-type cryomodules are used. Each cavity aims to provide $12.5\,\mathrm{MV\,m^{-1}}$ of accelerating field. To explain the interaction of electron beams with the cavities' field modes, the basics of RF cavities with emphasis on mode spectra and figure of merits of SRF cavities are described. Details on the behaviour of SC materials in the presence of high-frequency AC fields as well as other operational and design considerations can be found in the literature, for example see section 7.3.8 in [16].

4.1 Radio-Frequency (RF) Cavities

Following the description of waveguides in Ref. [28], a short description of RF cavities is presented. The propagation of electro-magnetic waves in waveguides can be described by the wave equation:

$$\Delta\vec{E} - \frac{1}{c^2}\frac{\partial^2}{\partial t^2}\vec{E} = 0. \tag{4.1}$$

For the understanding of the spatial distribution of the fields, only the time-independent part of the equation is needed. With the ansatz:

$$\vec{E}(\vec{r},t) = \vec{E}(r)\exp(i\omega t), \tag{4.2}$$

where $\vec{r} = (x, y, s)$, the spatial part, can be separated from the periodic part with frequency ω. Using this ansatz in Eq. 4.1 results in the time-independent wave equation:

$$\Delta\vec{E}(\vec{r}) + k^2\vec{E}(\vec{r}) = 0, \tag{4.3}$$

where $k = \frac{\omega}{c} = \frac{2\pi}{\lambda}$ is the wave number. The common solution for Eq. 4.1 can be written in the form:

$$W(\vec{r},t) = A\mathrm{e}^{i(\omega t+\vec{k}\vec{r})} + B\mathrm{e}^{i(\omega t-\vec{k}\vec{r})}, \tag{4.4}$$

which describes incident and reflected wave with amplitude A and B respectively. If a wave is fully reflected at a boundary, both amplitudes are equal

($A = B$) and Eq. 4.4 becomes:

$$\begin{aligned} W(\vec{r}, t) &= A\mathrm{e}^{i\omega t}(\mathrm{e}^{i\vec{k}\vec{r}} + \mathrm{e}^{-i\vec{k}\vec{r}}) \\ &= 2A\cos\left(\vec{k}\vec{r}\right)\mathrm{e}^{i\omega t}. \end{aligned} \tag{4.5}$$

The solution created by the two overlapping waves has a fixed amplitude $2A\cos\left(\vec{k}\vec{r}\right)$; it is a standing wave. That means there are also positions where the amplitude is 0, exactly when $\vec{k}\vec{r} = \left(n + \frac{1}{2}\right)\pi$, with $n \in \mathbb{N}$. Introducing perforated metallic walls at these positions does not change the field configuration. A standing wave can always exist in such a metallic cavity when the requirement of:

$$L_b = p\frac{\lambda_z}{2}, \quad \text{where} \quad p = 0, 1, 2, \ldots, \tag{4.6}$$

is fulfilled. A cavity behaves like a resonant circuit and can achieve high quality factors and small losses, which is their major advantage used for the generation of large accelerating voltages.

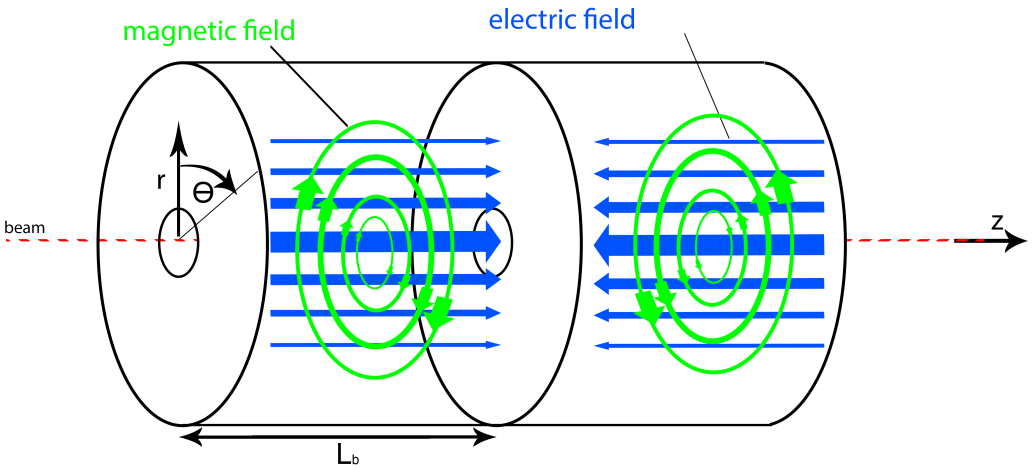

Figure 4.1: Cylindrical cavity with perforated metallic walls as can be used for acceleration [29].

4.1.1 Mode Spectra Inside a Cavity

With the boundary condition that all electric fields which are parallel to the cavity's surface must vanish on the surface as well as all magnetic field lines which are orthogonal to the cavity's surface vanish due to the eddy currents

on the surface, the possible field configurations inside the cavity can be calculated. Modes inside a cavity are denoted by three indices m, n, p for the three coordinates of a cylindrical coordinate system r, θ, z. The fundamental mode in accelerator physics is the transverse magnetic TM_{010} mode or accelerating mode, see Fig. 4.2, in which only transverse magnetic field lines occur, resulting in parallel electric field lines on axis, which are used for acceleration. Higher order modes (HOMs), e.g. TM_{110} (dipole mode), see Fig. 4.3, and TM_{210} (quadrupole mode), see Fig. 6.15, can be calculated for cylindrical cavities analytically. For more complex geometries, as for example the elliptical shaped TESLA cavities, numerical codes are available (e.g. CST Studio Suite, MAFIA, Poisson Superfish).

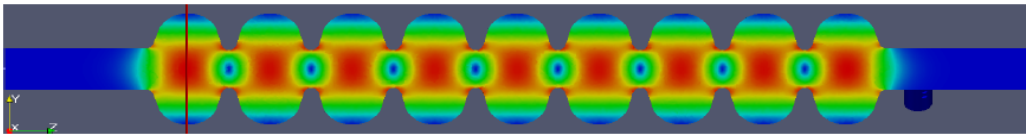

(a) $|\vec{E}|$ of the fundamental 1.3 GHz accelerating mode in a TESLA cavity.

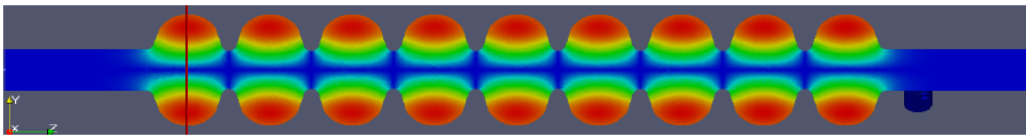

(b) $|\vec{B}|$ of the fundamental 1.3 GHz accelerating mode in a TESLA cavity.

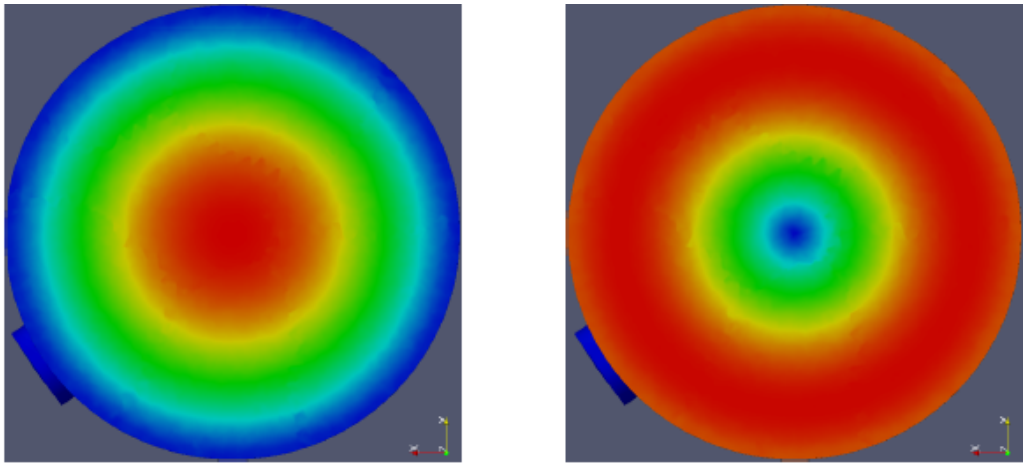

(c) Cut view of $|\vec{E}|$ (left) and $|\vec{B}|$ (right) at the red line indicated in Fig. 4.2a and 4.2b

Figure 4.2: Example of the fundamental 1.3 GHz accelerating mode (mode 9, π mode of the first passband) in a TESLA cavity taken from Ref. [30], simulated with CST Studio Suite.

In a multi-cell cavity, for each mode in a passband there exists a number of modes equal to the number of cavity cells. For example, for the TESLA cavity

there is the fundamental accelerating mode, the so-called π mode at 1.3 GHz. The field configuration of this mode is shown in Fig. 4.2. Close to the frequency of the fundamental mode, there are eight more modes denoted as $\frac{n\pi}{9}$, where $n = 1, \ldots, 8$. The naming scheme can be understood from the acceleration point of view. If we want to use 1.3 GHz for acceleration, a particle travelling with $v = c$ should see accelerating fields in each cavity cell. This means that the cavity phase has to change by 180° or π in the time it takes a particle to travel through one cell of the cavity to the next as was explained earlier and illustrated in Fig. 3.1 and Fig. 3.2.

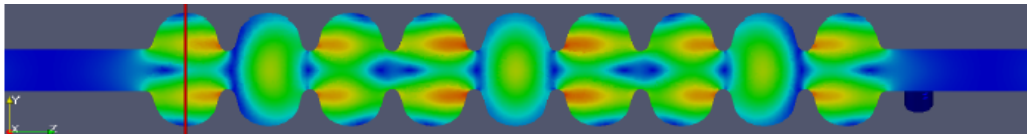

(a) $|\vec{E}|$ of a dipole HOM in a TESLA cavity.

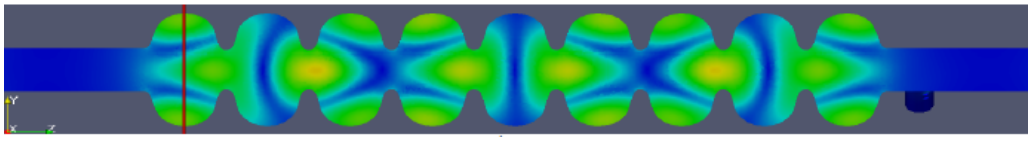

(b) $|\vec{B}|$ of a dipole HOM in a TESLA cavity.

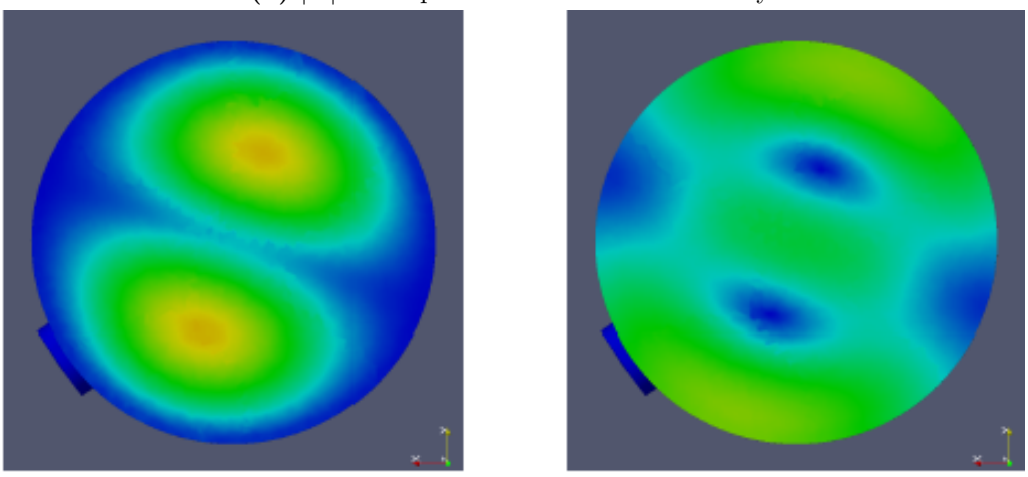

(c) Cut view of $|\vec{E}|$ (left) and $|\vec{B}|$ (right) at the red line indicated in Fig. 4.3a and 4.3b

Figure 4.3: Example of a dipole HOM (mode 7 of 2nd passband) in a TESLA cavity taken from Ref. [30], simulated with CST Studio Suite.

4.1.2 Figures of Merit

The characterisation of modes inside a cavity is done by three important parameters. First is the frequency at which the modes are excited, which is a sole property of the cavity design and which modes can exist in a given shape. Second is the quality factor or Q factor of that mode, which describes how under-damped the cavity is. A high Q factor is equal to a small bandwidth Δf at $-3\,\mathrm{dB}$, basically describing the time it takes the cavity to dissipate energy stored inside that mode through losses. The third important parameter is the so-called shunt impedance R/Q_0, which in the case of a monopole mode m = 0 (e.g. fundamental mode) is given by:

$$\frac{R}{Q_0} = \frac{\left|V_\parallel\right|^2}{\omega W},$$

where $V_\parallel$ is the voltage parallel to the longitudinal axis, ω is the mode's frequency and W the stored energy. It is a measure of how easily power can be transferred to the electric field of a certain mode. For the transverse shunt impedances, as it would be used to describe the modes with $m \geq 1$, the voltage of interest is the one that is perpendicular to the longitudinal axis:

$$\frac{R}{Q_{0\,\perp}} = \frac{|V_\perp|^2}{\omega W}.$$

The shunt impedance R/Q_0 is a purely geometric factor and is basically determined by the design of the cavity. Usually in the design stage, it is maximized for the fundamental accelerating mode and minimized for all others. For example in the TESLA type cavities, shunt impedances of HOMs can be in the order of 10 % of the shunt impedance of the fundamental mode [30].

4.2 TESLA-Type Cavities

For the MESA accelerator, superconducting cavities of the TESLA type are chosen. In several applications, such as the Tesla Test Facility (TTF) [31], the

European X-Ray Free-Electron Laser (E-XFEL) [32] and the Elektronen Linearbeschleuniger für Strahlen hoher Brillanz und niedriger Emittanz (ELBE) [33], a lot of experience was gained with the superconducting technology involved. Since the beginning of industrial large-scale production for the XFEL project, TESLA type cavities have been relatively easy to obtain. No additional design work for the cavities is necessary, and the projected accelerated gradients for MESA were easily exceeded by most of the XFEL cavities [34]. Due to the similiar nature of the ELBE facility, which operates in continuous wave operation, also the cryomodules for MESA were chosen to be of the ELBE type. The MESA modules include modifications of the HOM coupler antennas' thermal coupling properties as well as a fast piezo tuner [35]. Several tests have been performed at each stage of production. Tests of the two fabricated modules are currently still going on, while all of the project goals were already achieved in one cryomodule, e.g. 12.5 MeV at a Q of more then 1.25×10^{10} [36]. A CAD rendering of the cavities can be seen in Fig. 4.4.

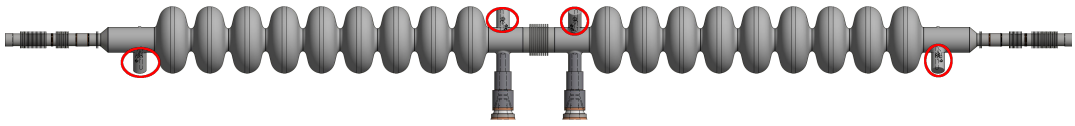

Figure 4.4: CAD Model of the MESA cavity string. The RF power is coupled in via two couplers located at the bottom center. Four additional HOM couplers (red circles) enable the coupling of HOMs out of the module via a hook antenna and a strip line, so that the HOM power can be damped outside the 2 K part of the module.

Each cryomodule consists of two TESLA-type 9-cell cavities connected at their so-called short ends via a bellows. At the long ends, a pickup antenna and a HOM coupler are mounted. In the center of the module, at the short ends of the cavities, two high-power (15 kW) couplers are used to supply the required RF power to drive the electro-magnetic fields inside each cavity. The whole cavity string is then welded into a titanium vessel, which houses the cryogenic bath during operation. Four more coupler ports are visible on the module, which house the HOM coupler antennas and provide the HOM damping capability of the cavities. A sketch of the HOM coupler can be seen in Fig. 4.5. Each cavity has two HOM couplers, which are rotated by 115° with respect to each other. In the two-cavity string, a total of four HOM couplers can extract energy from

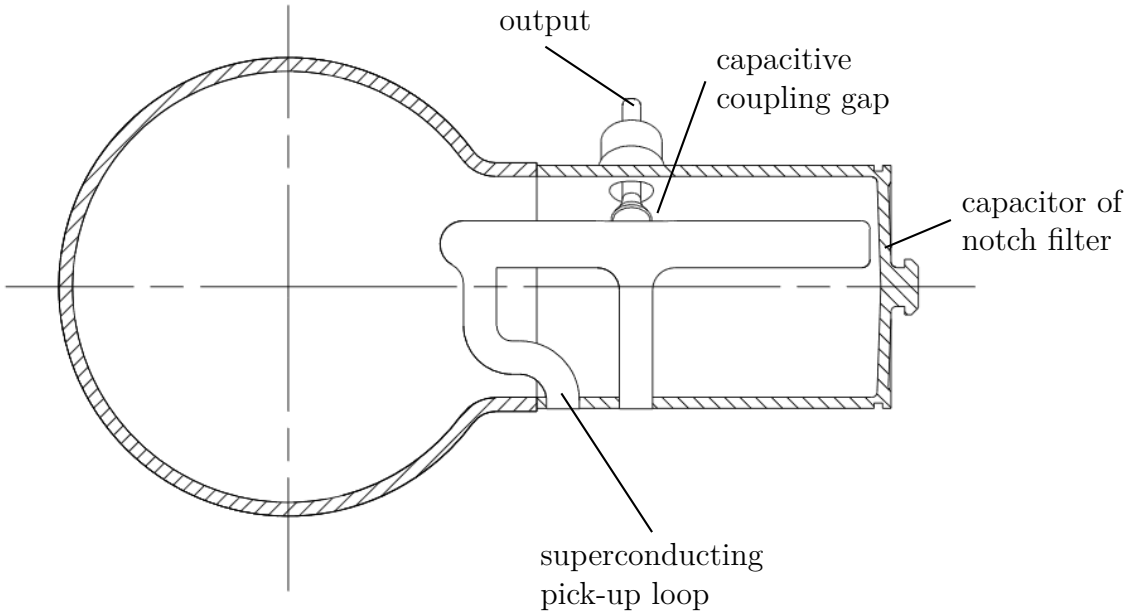

Figure 4.5: Cut view of the HOM coupler [31]. The superconducting pick-up loop is capacitively coupled to the output.

unwanted modes via a strip line to outside of the module in order to reduce the heat load on the cryogenic bath and to get rid of the HOMs' stored energy.

4.3 Cavity Edge Focussing Effects

One of the major beam dynamics effects that has to be accounted for in low-energy machines is the so-called cavity edge focussing as described in [37] in the case of ultra-relativistic particles $v \approx c$ and paraxial approximation. For a pure π-mode standing-wave accelerating cavity, the focussing in either transverse coordinate is described by:

$$\mathbf{R}_{\mathrm{tf}} = \begin{pmatrix} \cos\alpha - \sqrt{2}\cos\phi\sin\alpha & \frac{\sqrt{8}\gamma_0}{\Delta\gamma}\cos\phi\sin\alpha \\ -\frac{\Delta\gamma}{\gamma_1}\left(\frac{\cos\phi}{\sqrt{2}} + \frac{1}{\sqrt{8}\cos\phi}\right)\sin\alpha & \frac{\gamma_0}{\gamma_1}(\cos\alpha + \sqrt{2}\cos\phi\sin\alpha) \end{pmatrix}$$

where $\alpha = \frac{\sqrt{8}}{\cos\phi}\log\frac{\gamma_1}{\gamma_0}$, γ_0 and γ_1 are the initial and final relativistic gamma factors, $\Delta\gamma$ is the change of relativistic gamma factors along the structure and

ϕ is the phase of the particle with respect to the on-crest accelerating field. $\phi = 0$ would imply on-crest acceleration for the pure π-mode standing-wave cavity.

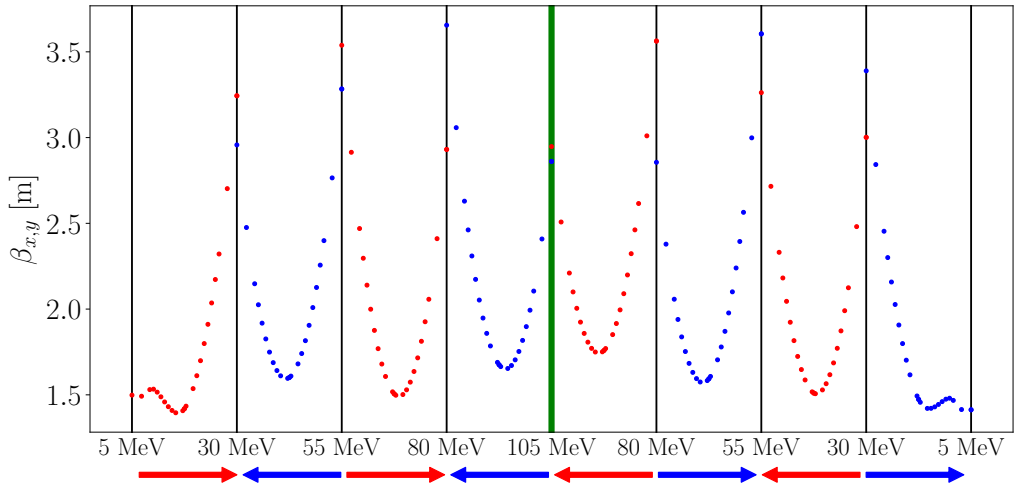

Figure 4.6: The beta functions along the accelerating cavities of MESA, showing all passes through each cryomodule with their respective energies. Red arrows indicate accelerating passes through a cavity, blue arrows indicate decelerating passes. The green line indicates the symmetry axis of MESA, separating all passes through the first cryomodule and through the second.

One of the major pitfalls of the design of a split-Linac ERL is shown in Fig. 4.6, the fact that cavity edge focussing is energy dependent but accelerating and decelerating beams use the same optics, so passes cannot be tuned individually. The left half of the plot shows all the passes of particle bunches through the first cryomodule, alternating between accelerating and decelerating passes. The right half shows all the passes through the second cryomodule. The blue and red arrows indicate accelerating and decelerating passes, respectively. For example, the first red arrow describes the first accelerating pass through the first cryomodule from 5 MeV to 30 MeV, while the blue arrow shows the decelerating pass. For the second cryomodule the situation is inverted: the first red arrow of the second half indicates the accelerating pass through the second cryomodule from 80 MeV to 105 MeV. At the black lines, indicating the start and end of the cryomodule, respectively, the beta functions should be identical in a perfectly aligned machine. The first cryomodule was matched by means of the FMC arc to perfectly match the arc (MARC1) after the cryomodule. This procedure could not easily be applied to all passes, since changing the optics on

the accelerating passes directly impacts the optics on the decelerating passes. Since the optics design is not yet finalized, the matching of the cavities is still in progress. However it should be noted that this not yet fully optimized setup would already be able to accelerate and decelerate the 10 mA beam without beam loss.

4.4 ERL Start-to-End Simulation

The MESA lattice was developed by D. Simon using BeamOptics, MAD-X and Parmela. For the extraction of transport matrices of the arcs and to perform start-to-end simulations, the arc optics were translated from MAD-X to ELEGANT and the SRF cavities are implemented into the lattice.

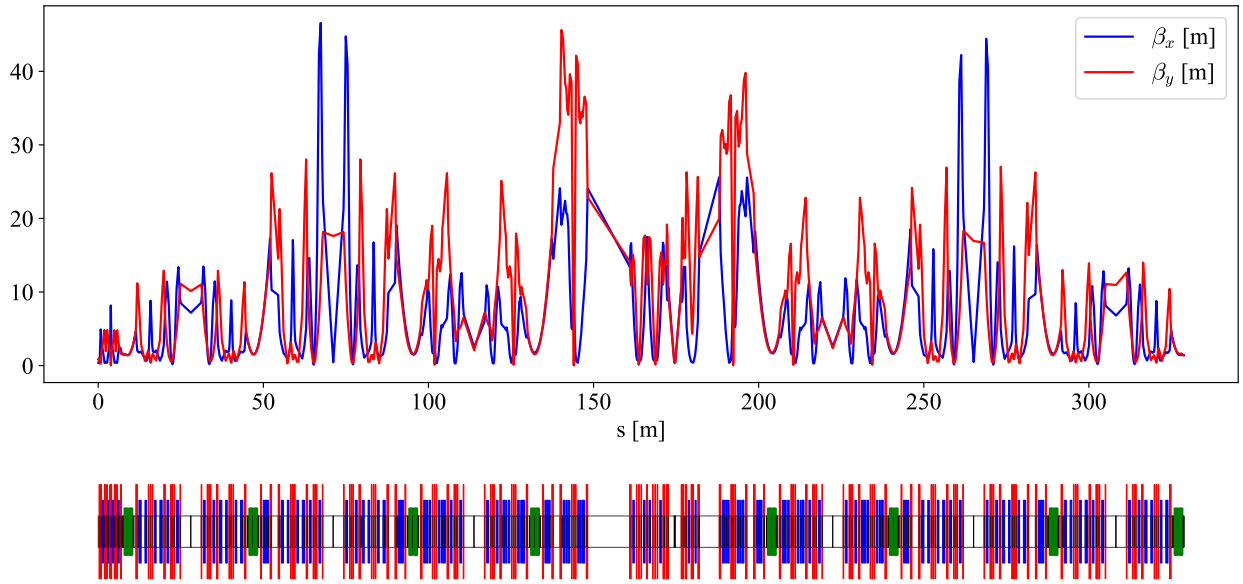

Figure 4.7: Simulation results of the horizontal and vertical beta functions along the ERL lattice. The coloured boxes below depict the optical elements along the beamline. Quadrupoles are red, dipoles blue and cavities green.

Additionally, a 5 MeV injection arc was designed and matched to the first cryomodule for ER operation considering beam parameters from previous source-to-injector simulations. The injection arc was designed as a flexible momen-

tum compaction (FMC) arc. It consists of four dipole magnets, where four quadrupole magnets can match the beam from the injector into the injection arc. There are additional quadrupole magnets, which enable enough flexibility to set the momentum compaction R_{56} to a desired value for both of the planned operation modes and also be able to adjust for different non-isochronous recirculation modes, which might be helpful in increasing the stability of the ER mode [38]. Another problem that arises with low-energy beam transport is that the beam size is intensity dependent. Calculations of the influence of space charge (SC) on the beam and mitigation of the effects observed were done in collaboration with A. Khan and published in [22].

As can be seen, the initial matching of the beta functions works nicely but is slightly asymmetric due to effects from non-ultra-relativistic energies of the electron beam in the cryomodule. A focus of the beam should be achieved at the experiment, with an energy spread as low as possible at the order of 5×10^{-4}. While performing the start-to-end simulations for the beam break up studies, also the phase space at the experiment was investigated. With the chirped bunch and the bunch compressor without further optimization, an energy spread of 4.76×10^{-4} at the experiment was achieved. For further improvement of the energy spread, longitudinal working points with off-crest acceleration and deceleration are considered as well [38]. This implies additional investigations on mode excitation in the future.

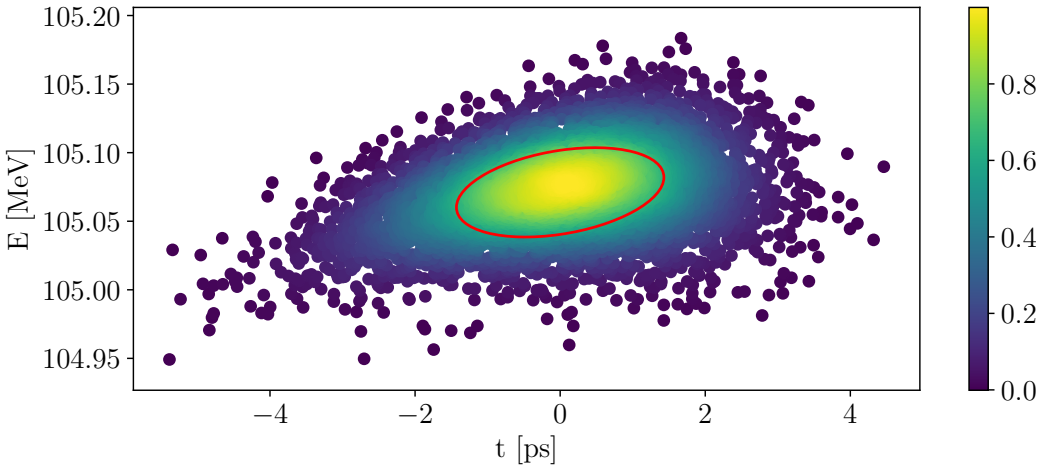

Figure 4.8: Longitudinal phase space at the position of the internal-target experiment using a chirped bunch and using the injection arc as a bunch compressor with non-zero momentum compaction R_{56}. The red ellipse denotes the 1σ area the beam occupies.

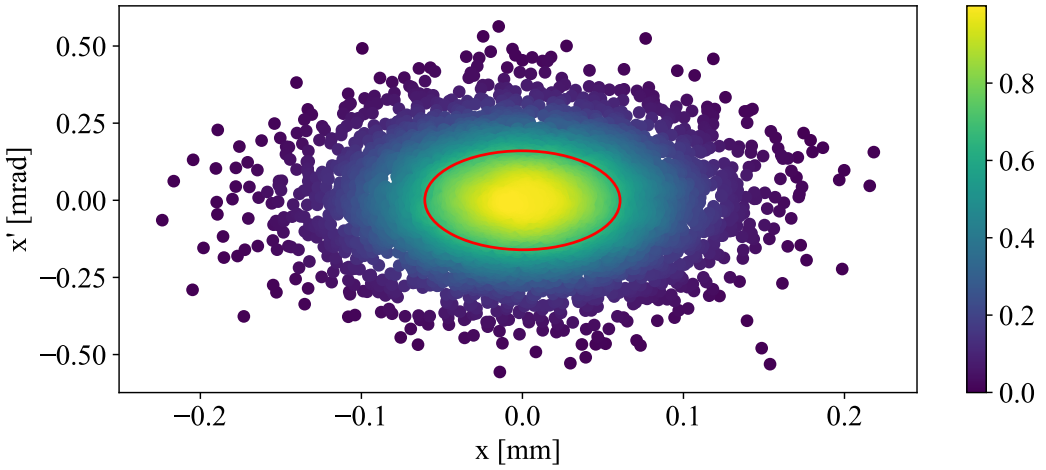

Figure 4.9: Horizontal phase space at the position of the internal-target experiment. The red ellipse denotes the 1σ area the beam occupies.

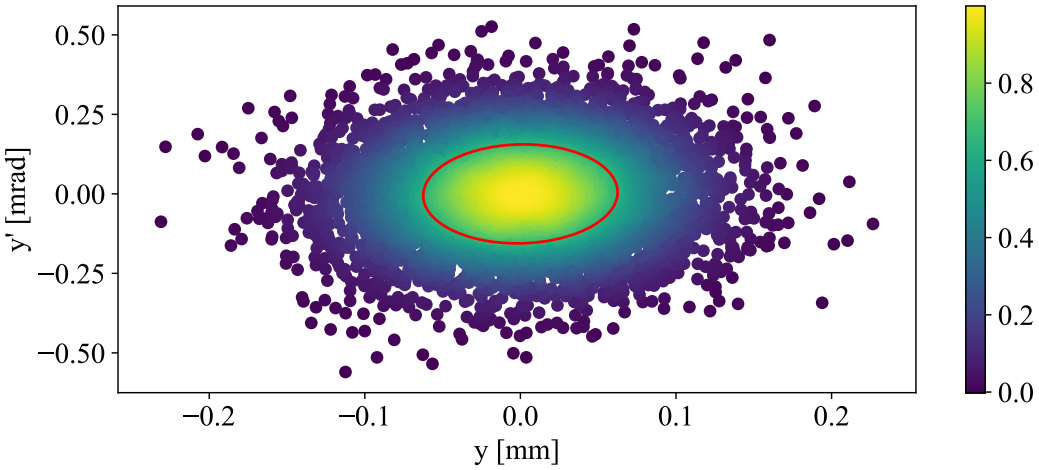

Figure 4.10: Vertical phase space at the position of the internal-target experiment. The red ellipse denotes the 1σ area the beam occupies.

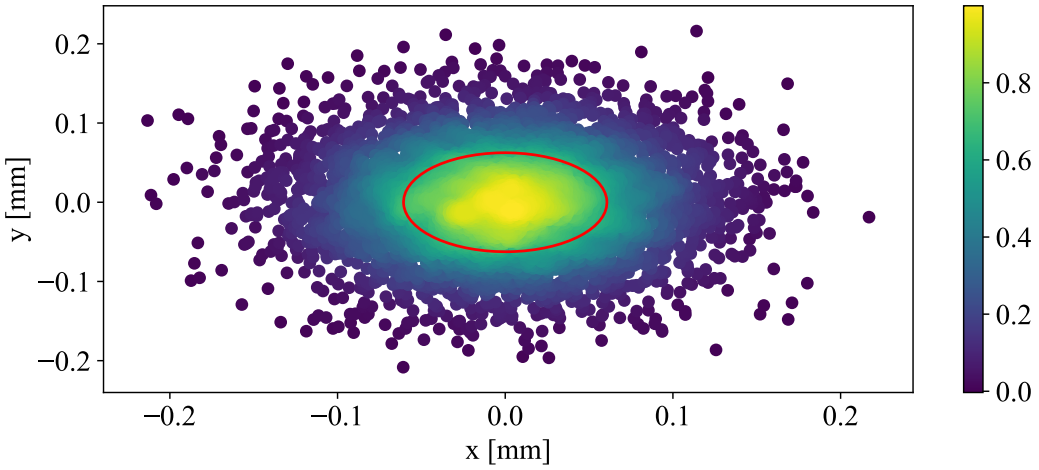

Figure 4.11: The x-y phase space at the position of the internal-target experiment. The red ellipse denotes the 1σ area the beam occupies.

5 Beam Breakup Instability

The effect of the Beam Breakup instability (BBU) was first reported for a number of short high-current Linacs and closely investigated for the Stanford linear accelerator (SLAC) [39] in 1966. An instability that leads to beam loss was observed when the beam current was increased above a certain threshold. The instability could be related to beam interactions with higher-order TM_{110}-modes (dipole HOMs) excited by the beam. Due to the accelerator's length of about 3 km and the transversely deflecting character of the excited mode, a small deflection at the beginning of the accelerator could lead to a stronger HOM excitation in subsequent cavities. Following bunches would then receive a stronger transverse kick, increasing the HOM excitation in subsequent cavities. Finally, when the HOM excitation in one of the cavities would cause beam loss, the accelerator would be shut down to prevent machine damage. It was observed that this instability only occurred with certain bunch patterns and above a certain beam current. This threshold current was found to be 14 µA, and therefore only half of the initial design current of 30 µA was available.

The phenomenon described here is called cumulative BBU as it is a result of compounding beam deflections that add up for a long array of accelerating structures, where some initial transverse offset of the bunches can lead to increasing HOM excitation, which can finally lead to beam loss. Countermeasures implemented at SLAC included careful detuning of some of the cavities to change the HOM frequencies between neighbouring cavities' TM_{110}-modes (inducing frequency spread) and thereby increasing the threshold current by $\approx$ 30 % [40].

Since then, cavities for high-current applications have been carefully designed to take into consideration the effect of HOM interaction with the beam, but it has yet to be shown that there is the possibility of CW operation with very high currents in the order of several hundred mA as it is required for electron cooler applications of ERLs [41]. For pulsed machines, such as the 1.7 km long european X-Ray Free Electron Laser (XFEL), the problem of BBU is also mitigated by applying certain bunch patterns in combination with HOM damped cavities.

For MESA, the TESLA-type cavities chosen are not optimised for CW operation, but have been modified to allow for high-current ($\approx 1\,\mathrm{mA}$), CW operation. In the following section, the Beam Breakup instability for multi-pass, energy recovery and CW configurations will be presented.

5.1 Multi-pass BBU in ERLs

While cumulative BBU is mostly present in long Linacs, in recirculating Linacs such as ERLs another type of BBU instability usually dominates, since the accelerating sections are shorter but passed multiple times. The so-called regenerative BBU occurs when a coupling mechanism between the beam and a cavity's HOMs is established.

5.1.1 Regenerative BBU Theory

The fundamental interaction mechanism of regenerative BBU is the coupling of the beam to the electromagnetic field components of a dipole higher-order mode. An electron bunch loses energy to the dipole HOM's electric field and is deflected by the magnetic field component. If the energy loss of the beam to the dipole mode is higher than the natural damping of that mode, the instability develops. Any steering error or non-uniform beam distribution feeds power to these modes. Also, HOMs can be excited by the fundamental power coupler

itself, so a HOM is never 100 % suppressed even with a perfectly aligned beam. Subsequent bunches can then be deflected by the transverse magnetic field of the HOM and start to oscillate around the reference orbit. If the bunches arrive back at the cavity with a transverse offset, a positive feedback loop is established, so that more and more power is fed to the HOM and the beam is deflected out of the accelerator acceptance. This can already impede machine operation when beam halo is deflected into the superconducting cavities. Here the amount of power that can be thermally lost in the cavity walls is limited, since it has to be removed by the cryogenic system and can result in a quench (thermal breakdown of superconductivity) of the cavity.

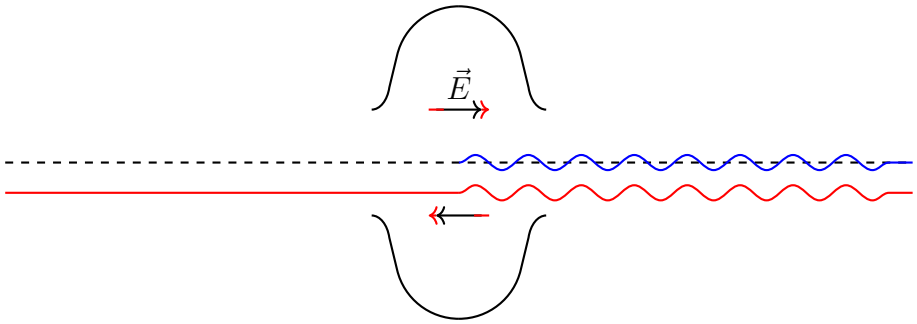

Figure 5.1: Orbit deviation (blue) from the reference orbit (dashed black) induced by a dipole HOM. An initial kick given to the beam from a HOM can translate into a transverse offset that oscillates around the reference orbit. If the beam enters the cavity with a transverse offset (red), additional power can be fed to the HOM, resulting in larger deflection for subsequent particles.

Following the description for two-dimensional regenerative BBU given in Ref. [42], a formula for the maximum achievable threshold current can be derived in the case of a single cavity, with low bunch charge (resulting in low energy exchange to the HOM) and where the frequency of the HOM is not a multiple of the bunch repetition rate. Arrival times with respect to the HOM phase are expected to be randomly distributed in the interval of $[0, 2\pi]$. The energy change ΔU in a dipole HOM produced by a point-like bunch ΔU in the one-dimensional case is given by [43]:

$$\Delta U = -qV_a \cos(\phi)\frac{x}{a}, \tag{5.1}$$

where V_a is the accelerating HOM voltage at the radius of the beam pipe a induced by previous bunches, ϕ is the phase of the point-like bunch with respect

to the peak of the HOM field, and q is the bunch charge. For a two-dimensional description of the problem, the offset x has to be mapped to the projection of the beam displacement vector $\vec{d}$ on the vector of mode polarisation $\vec{n}$:

$$x \to \vec{d} \cdot \vec{n} = x\cos(\alpha) + y\sin(\alpha), \tag{5.2}$$

where $\vec{d}$ is the displacement vector (x, y) and α is the mode polarisation angle in the x, y plane. The energy deposited in the HOM on the first and second passes can be written as:

$$\Delta U_1 = -q\frac{V_a}{a}\cos(\phi)[x_1\cos(\alpha) + y_1\sin(\alpha)], \tag{5.3}$$

$$\Delta U_2 = -q\frac{V_a}{a}\cos(\phi + \omega T_r)[x_2\cos(\alpha) + y_2\sin(\alpha)], \tag{5.4}$$

where T_r is the recirculation time. The underlying assumption here is that the voltage V_a of the HOM does not change significantly during recirculation. The coordinates of the recirculated bunch, x_2 and y_2, can be expressed via the bunch coordinates before deflection and the HOM accelerating voltage on the first pass as:

$$x_2 = m_{11}x_1 + m_{12}x_1' + m_{13}y_1 + m_{14}y_1' - \frac{qV_a}{\omega ap}\sin(\phi)[m_{12}\cos(\alpha) + m_{14}\sin(\alpha)], \tag{5.5}$$

$$y_2 = m_{31}x_1 + m_{32}x_1' + m_{33}y_1 + m_{34}y_1' - \frac{qV_a}{\omega ap}\sin(\phi)[m_{32}\cos(\alpha) + m_{34}\sin(\alpha)], \tag{5.6}$$

where p is the beam momentum and m_{ij} are the mapping matrix elements. The deflection angle produced by the HOM is expressed via the accelerating HOM voltage V_a and its phase ϕ as [43]:

$$x' = -\frac{eV_a}{\omega ap}\sin(\phi)\cos(\alpha), \tag{5.7}$$

$$y' = -\frac{eV_a}{\omega ap}\sin(\phi)\sin(\alpha). \tag{5.8}$$

The average power deposited by the beam $\dot{U}_{\text{beam}}$ in the HOM is equal to the average energy deposited by individual bunches times the bunch repetition frequency f_b:

$$\dot{U}_{\text{beam}} = \langle \Delta U_1 + \Delta U_2 \rangle f_b. \tag{5.9}$$

Here, the averaging in Eq. 5.9 is done with respect to the phase ϕ of the HOM, taken at moments when bunches pass through the cavity on the first pass. Ohmic losses in the cavity can be expressed as [43]:

$$P_c = \frac{V_a^2}{\left(\frac{\omega}{c}\right)^2 a^2 \left(\frac{R_d}{Q_0}\right) Q_L}. \tag{5.10}$$

The energy balance equation for the HOM stored energy is:

$$\dot{U} = \dot{U}_{\text{beam}} - P_c = \langle \Delta U_1 + \Delta U_2 \rangle f_b - P_c. \tag{5.11}$$

Inserting Eq. 5.3 and Eq. 5.4 into Eq. 5.11 and averaging, terms proportional to $\cos(\phi)$, $\sin(\phi)$, $\cos(\phi + \omega T_r)$ and $\sin(\phi + \omega T_r)$ yield zero if x_1, x_1' and y_2, y_2' are steering/misalignment errors. If the HOM frequency is not a harmonic of the bunch repetition rate, terms proportional to $\cos(\phi)\sin(\phi)$ also yield zero. Thus, Eq. 5.11 can be written as:

$$\dot{U} = f_b q \frac{eV_a^2}{\omega p a^2} M^* \langle \sin(\phi)\cos(\phi + \omega T_r) \rangle - \frac{V_a^2}{(\omega/c)^2 a^2 (R_d/Q_0) Q_L}. \tag{5.12}$$

The term $\langle \sin(\phi)\cos(\phi + \omega T_r) \rangle$ in the above equation, can be expanded to:

$$\langle \sin(\phi)\cos(\phi)\cos(\omega T_r) - \sin(\phi)^2 \sin(\omega T_r) \rangle. \tag{5.13}$$

The first term in Eq. 5.13 yields zero on average, and the average of $\sin(\phi)^2$ is $\frac{1}{2}$. This leads to:

$$\dot{U} = -I_b \frac{eV_a^2}{\omega p a^2} M^* \frac{\sin(\omega T_r)}{2} - \frac{V_a^2}{(\omega/c)^2 a^2 (R_d/Q_0) Q_L}, \tag{5.14}$$

where I_b is the product of the bunch charge and the bunch repetition rate. $\dot{U}$ is equal to zero at the threshold; thus, the threshold current is given by:

$$-I_{\text{th}} \frac{e}{\omega} \frac{M^*}{2p} \sin(\omega T_r) - \frac{1}{(\omega/c)^2 (R_d/Q_0) Q_L} = 0. \tag{5.15}$$

The maximum achievable threshold current before BBU occurs in a given machine can then be described as:

$$I_{\mathrm{th}} = \frac{-2pc}{e\left(\frac{R_d}{Q_0}\right)_m Q_{L,m} k_m M^* \sin(\omega_m T_r)}, \tag{5.16}$$

where p is the particle momentum, T_r is the recirculation time, $(R_d/Q_0)_m$ is the shunt impedance of the HOM m, $Q_{L,m}$ is the loaded quality factor of mode m and k_m is the wave number of mode m, ω_m is the frequency of mode m, and the parameter:

$$M^* = m_{12}\cos^2(\alpha) + (m_{14} + m_{32})\cos(\alpha)\sin(\alpha) + m_{34}\sin^2(\alpha), \tag{5.17}$$

is the matrix element which maps transverse momenta to transverse positions from the end of the cavity back to the entrance, for example m_{12} maps the deflection x' to the offset in x. Here, α is the polarisation of the HOM in question. This approximation formula is very helpful in finding the most critical parameters that limit the achievable threshold current, though it will not be used for quantitative analysis. These parameters are:

- R/Q_0, the shunt impedance of the cavity, which for the HOMs is already determined in the cavity design stage and should be as low as possible.

- Q_L, the loaded quality factor of the HOM, which is also minimized in the design stage but is subject to change after cavity fabrication and incorporation into the cryomodule.

- The momentum of the bunches p, which already shows that the most critical cavity is the one that sees beams with the lowest momenta.

- The polarisation mapping matrix element M^*, which also contains the information about the HOM polarisation. Depending on the amplitude of the matrix elements m_{ij} which represent the optics layout of the accelerator, certain polarisations can have a more severe impact on the threshold current. For a machine with uncoupled optics depending on

the amplitude of m_{12} and m_{34}, either polarisations of 0° or 90° have the biggest impact.

5.1.2 Regenerative BBU in ERLs

In 2004, Hoffstaetter and Bazarov extended the formalism of BBU instability to arbitrary bunch patterns including ERL operation [44]. Following their description, the basic ideas and assumptions made will be presented in this section. If a current $I(t')$ passes through a cavity, the charge $I(t')\mathrm{d}t'$ excites a dipole HOM. Subsequent particles travelling through that cavity at time t experience a kick by the HOM:

$$\Delta p_x(t) = \frac{e}{c} W(t-t')x(t')I(t')\mathrm{d}t'. \tag{5.18}$$

The wake function $W(\tau)$ describes the transverse force at the time τ after the HOM is excited. Momentum transfer from the HOM to the bunch is described by an effective transverse voltage of the HOM:

$$V(t) = \frac{c}{e}\Delta p_x(t). \tag{5.19}$$

The effective transverse voltage of the HOM determines the kick $\Delta p_x(t)$ that a bunch sees, and what position it will have after the recirculation time t_r when it enters the cavity again. The transfer matrix element T_{12} maps the transverse momentum to the transverse position:

$$x(t+t_r) = T_{12}p_x(t).$$

Inserting the above expression and Eq. 5.18 into Eq. 5.19 yields an integral equation for the HOM's effective voltage:

$$V(t) = \int_{-\infty}^{t} W(t-t')I(t')T_{12}\frac{e}{c}V(t'-t_r)\mathrm{d}t' \tag{5.20}$$

Assuming a CW beam with bunch spacing t_b, the current can be expressed as a string of equidistant charges:

$$I(t) = I_0 t_b \sum_{m=-\infty}^{\infty} \delta_D(t - t_r - m t_b),$$

where δ_D is the Dirac-delta function and t_b is an integer multiply of the RF circulation time $t_0 = 2\pi/\omega_0$. It should be noted here that due to scaling of the Dirac-delta function:

$$\delta_D(a(x - x')) = \frac{1}{|a|}\delta_D(x - x'), \tag{5.21}$$

the unit of the Dirac delta function is one over the unit of its argument. The recirculation time is expressed in terms of t_b as:

$$t_r = (n_r - \delta)t_b,$$

with an integer n_r and $\delta \in [0, 1)$. For a recirculating Linac, $\delta t_b \approx n t_0$, meaning that the recirculation time is an integer multiple of the RF period. For an ERL $\delta t_b \approx (n + \frac{1}{2})t_0$, where the additional factor of $\frac{1}{2}$ is a result of the 180° phase slippage for the decelerating passes. The HOM voltage at a time $t \in [n t_b + t_r, n t_b + t_r + t_b)$ between two bunches can be written as:

$$V(t) = I_0 t_b T_{12} \frac{e}{c} \sum_{m=-\infty}^{n} W(t - t_r - m t_b) V(m t_b).$$

Evaluating this equation at $t = n t_b + t_r$, when the recirculated bunch passes through the cavity, leads to:

$$V(n t_b + t_r) = I_0 t_b T_{12} \frac{e}{c} \sum_{m=0}^{\infty} W(m t_b) V([n - m] t_b).$$

In CW recirculator theory, this equation was solved by treating the voltage as: $V(t) = V_0 \mathrm{e}^{-i\omega t}$ for $t = n t_b$, where a positive imaginary part indicates instability. Using this description of the voltage results in a formula for the threshold:

$$\frac{1}{I_0} = t_b T_{12} \frac{e}{c} \mathrm{e}^{i\omega t_r} \sum_{m=0}^{\infty} W(m t_b) \mathrm{e}^{i\omega m t_b}. \tag{5.22}$$

The smallest value of I_0 for which there is a real ω indicates the threshold of the instability. To allow for arbitrary recirculating configurations, $V(t)$ is written in form of its Laplace transform, which yields a different dispersion relation between I_0 and ω that can be used for all δ, and finally the threshold can be found from:

$$\frac{1}{I_0} = t_b T_{12} \frac{e}{c} \mathrm{e}^{i\omega n_r t_b} \sum_{n=0}^{\infty} W([n+\delta]t_b)\mathrm{e}^{i\omega n t_b}. \tag{5.23}$$

Using the far-field approximation of the wake function $W(\tau)$:

$$W(\tau) = \left(\frac{R}{Q}\right)_\lambda \frac{\omega_\lambda^2}{2c} \mathrm{e}^{-(\omega_\lambda/2Q_\lambda)\tau} \sin(\omega_\lambda \tau),$$

the sum in the dispersion relation can be evaluated. With $\omega_\lambda^\pm = \omega_\lambda \pm i(\omega_\lambda/2Q_\lambda)$ and $\omega^+ = \omega + i(\omega_\lambda/2Q_\lambda)$, the dispersion relation is written as:

$$I_0(\omega) = \frac{2}{KT_{12}} \mathrm{e}^{-i\omega n_r t_b} \frac{\mathrm{e}^{(\omega_\lambda/2Q_\lambda)\delta t_b}[\cos(\omega^+ t_b) - \cos(\omega_\lambda t_b)]}{\mathrm{e}^{-i\omega^+ t_b}\sin(\delta\omega_\lambda t_b) - \sin([\delta-1]\omega_\lambda t_b)}, \tag{5.24}$$

with $K = t_b(e/c^2)(R/Q)_\lambda(\omega_\lambda^2/2)$. For $\delta = 0$, this is the dispersion relation of the CW recirculator BBU theory:

$$I_0(\omega) = \frac{2}{KT_{12}} \mathrm{e}^{-i\omega t_r} \frac{\cos(\omega^+ t_b) - \cos(\omega_\lambda t_b)}{\sin(\omega_\lambda t_b)}.$$

This formula applies to the case where the recirculated bunches are in the same buckets as the accelerated ones. When the recirculated bunches are just between accelerated bunches as in an ERL, then $\delta = \frac{1}{2}$:

$$I_0 = \frac{2}{KT_{12}} \mathrm{e}^{-i\omega t_r} \frac{\cos(\omega^+ t_b) - \cos(\omega_\lambda t_b)}{\cos(\omega^+ t_b/2)\sin(\omega_\lambda t_b/2)}. \tag{5.25}$$

If every bucket is filled, this describes an ERL with $t_b = t_0$. With the effect of phase slippage in mind, one could think about configurations where the decelerating and accelerating bunches are not perfectly centered between each other. This case could be solved for $\delta t_b = (n + \frac{1}{2})t_0$ by using Eq. 5.24.

The threshold current above which the beam motion becomes unstable in the accelerator is the smallest current I_0 for which there is a real ω that satisfies the dispersion relation. To obtain the initial approximated formula from this

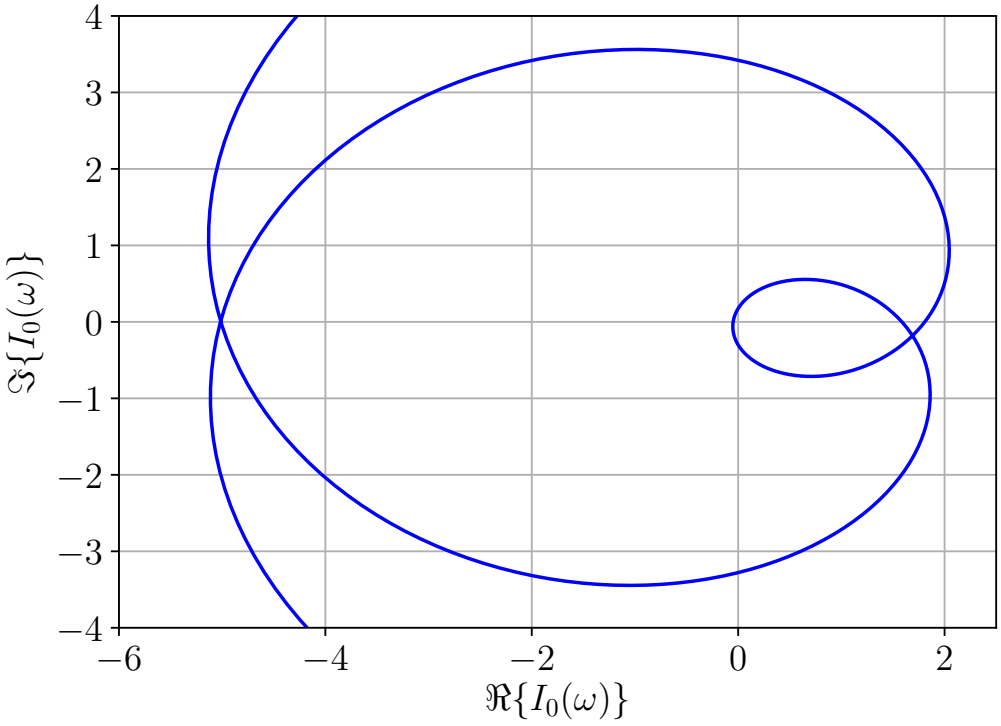

Figure 5.2: $I_0(\omega)$ in the complex plane for a sweep of $\omega \in [0, \pi/t_b)]$ on an arbitrary scale. The smallest, positive real value of I_0, i.e. the intersection with the real axis, is the threshold current.

relation, only a linearisation in $\epsilon = (\omega_\lambda/2Q_\lambda)t_b$ for $\epsilon \ll 1$ is required, which describes a situation where the HOM decay time is negligible at the time scale of the bunch spacing t_b, as is the case in CW Linacs and ERLs. Thus Eq. 5.24 reduces to:

$$I_0 = -\frac{\epsilon}{K}\frac{2}{T_{12}\sin(\omega_\lambda t_r)}. \tag{5.26}$$

Inserting the definitions of K and ϵ and using the definitions $k_\lambda = \frac{\omega_\lambda}{c}$, $T_{12} = \frac{m_{12}}{p}$, the approximation formula Eq. 5.16 derived earlier is reproduced. Using the same approximations as for Eq. 5.26, a formula for multi-turn ERLs can be derived:

$$I_{\text{th}}^{N_r} = -\frac{2c^2}{e\left(\frac{R}{Q_0}\right)_\lambda Q_\lambda \omega_\lambda}\frac{1}{\sum_{J=1}^{N_p}\sum_{I=J+1}^{N_p} T^{IJ}\sin(\omega_\lambda[t^I - t^J])}, \tag{5.27}$$

where N_p is the number of passes, N_r the number of recirculations and all parameters indexed with I, J refer to one pass. Summation over all passes yields the threshold current for multipass ERLs. It is interesting to investigate this formula a bit further. Usually, when two beams are recirculated, half the maximum threshold current would be expected. From the formula it can be assumed that the threshold current scales with $N_r(2N_r - 1)$ where N_r is the number of recirculations. From Ref. [44], it can in general be expected to decrease quadratically with N_r.

5.1.3 The Effect of Cavity Frequency Spread

In reality, each cavity is fabricated with slight differences in its geometry, directly impacting the associated dipole pair frequency spread, Q factors and Q factor scatter of the HOMs. Cavities are tuned to the fundamental mode at 1.3 GHz. The major effects of cavity imperfection on dipole modes are frequency shift, increase in dipole pair frequency separation, and Q factor scatter [45]. Frequency spread is beneficial to achieve higher threshold currents, since it reduces the possible crosstalk between the cavities. If each HOM of each cavity has a slightly different frequency, it decouples the system. For polarized HOMs, it is expected that a frequency spread larger than 1 MHz is beneficial. It was shown in studies for CBETA [46] as well as for MESA [47] that larger frequency spread can be very beneficial in increasing the threshold current. This was also experimentally shown for SLAC in the case of regenerative BBU. For MESA, the frequencies of both polarisations of the first 18 dipole modes have been measured and the results are presented in the next chapter.

5.1.4 The Effect of Q Spread

As discussed, each cavity can have different frequencies for its HOMs. The same is true for the bandwidth. This results in different Q values for each individual cavity and each individual HOM. In reality, BBU occurs at the cavity with the lowest threshold current, meaning that the accelerator current is usually

limited by its "weakest" component, e.g. highest Q HOM housing cavity. This was experimentally observed at JLAB and reported in [48]. The critical HOM was identified already prior to the measurements and, by carefully controlling all cavities, it was possible to find out exactly which cavity triggered the BBU instability (the one cavity that had the highest Q HOM at the BBU triggering frequency for that measurement).

6 BBU Threshold Current Limits for MESA

6.1 HOM Characterisation of the MESA SRF Cavities

As described in chapter 5, knowledge of the properties of HOMs of all four cavities is necessary to obtain the threshold current values for MESA. Since the ELBE-type cryomodules are equipped with two HOM couplers per cavity, the HOM characteristics can be obtained easily once the cavity is cooled down to 1.8 K and tuned to the fundamental 1.3 GHz mode. It was also possible to measure the HOMs before the cavities were mounted into the cryomodule, which leaves the opportunity to observe the changes from undressed to dressed cryomodule.

6.1.1 Simulation of the HOM Spectra

For the TESLA type cavity geometry, extensive simulations of the HOMs were performed, for example in Ref. [30]. If simulation data in the context of HOMs is mentioned, it always refers to this mode atlas containing a total of 194 HOMs simulated up to 3.2 GHz, including 86 dipole HOMs. The simulations were performed with consideration of the HOM damping abilities of the HOM couplers, but only for a single cavity with infinitely long beam tubes as boundary conditions. It should be noted that each dipole mode in an elliptical cavity can

have two polarisations, with slightly different frequencies. Depending on the cavity geometry, the Q values of the two modes might differ strongly from one another. This will be called Q spread for the rest of this work.

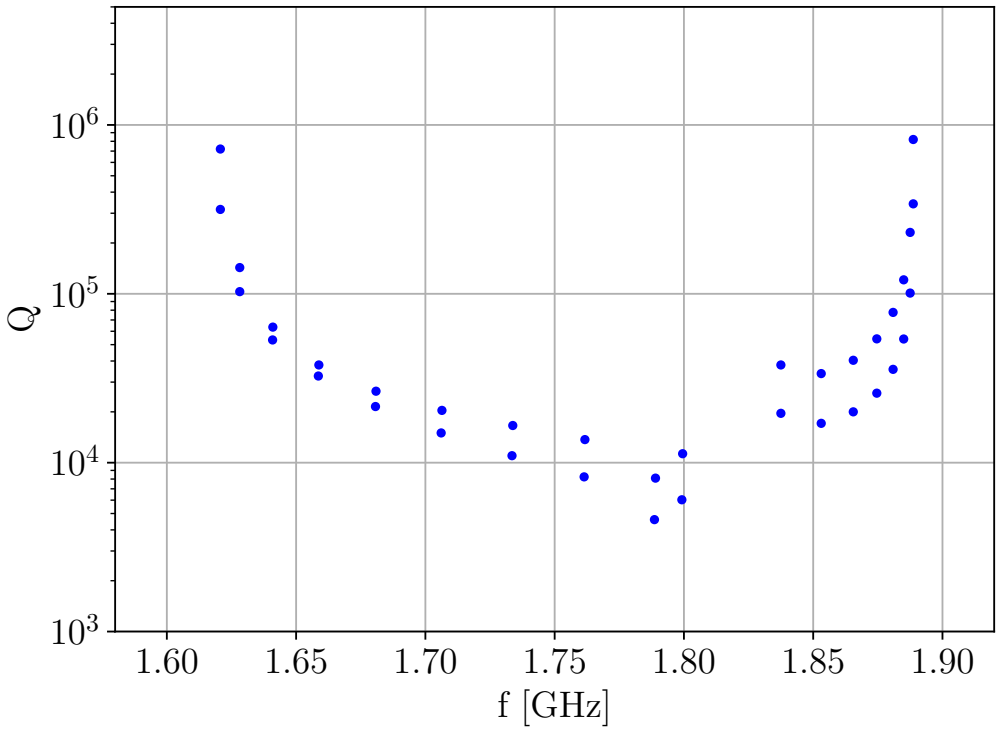

Figure 6.1: Q values of the first two passbands of dipole HOMs as simulated and presented in Ref. [30]. The Q spread between the two different polarisations is clearly visible.

6.1.2 Measurement of the HOM Spectra at DESY

As part of the quality control process for the cavity fabrication, all MESA 9-cell cavities were tested inside a vertical cryostat at DESY [49] before integration into the cryomodule. Figure 6.2 shows the relative frequency deviation between single modes from one cavity to another. MESA cavities are numbered from 7 to 10 by the vendor, being part of a series production for different institutes. As described in chapter 5, frequency spread between HOMs is a beneficial effect in terms of the maximum beam current one can transport. Since the cavities cannot be tuned to the fundamental mode in the vertical test setup, they are

expected to change their HOM frequencies when dressed inside the cryomodule. It is interesting to investigate if all cavities change their HOM frequencies in the same way, or if there is a change of the frequency spread associated with the tuning to the fundamental mode. The most important property related to

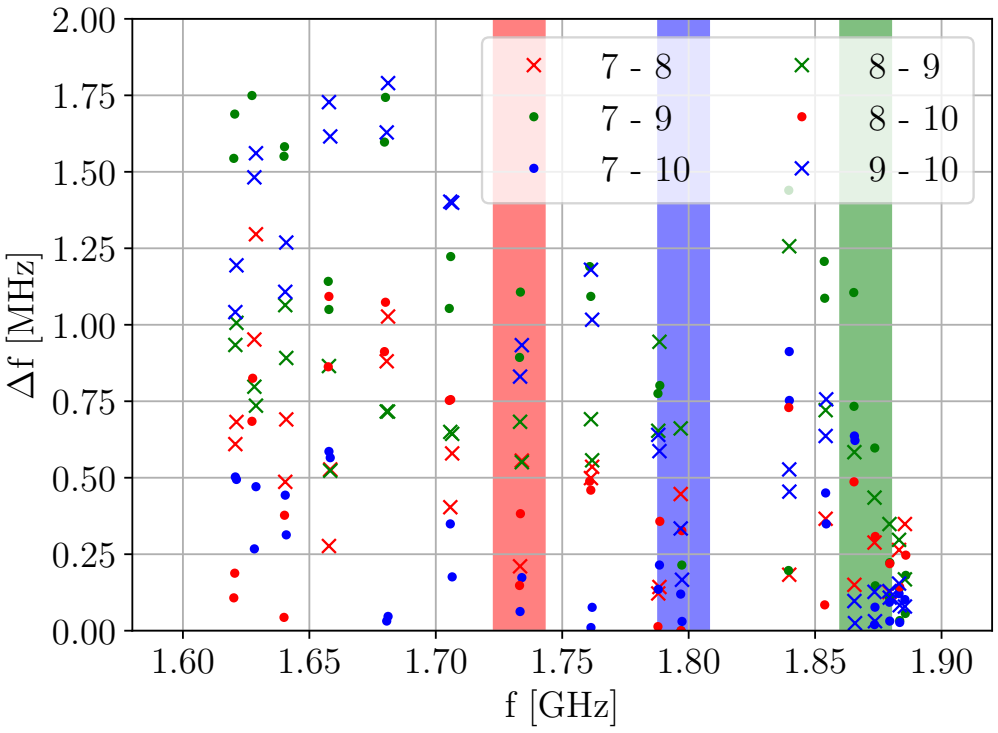

Figure 6.2: Investigation of frequency spread for the data obtained at DESY, where the cavities were measured in a vertical cryostat. The maximum observed frequency spread is 1.78 MHz.

BBU is the Q value of the HOMs. It was measured for all four cavities, while sometimes it was impossible to distinguish between the two polarized modes as their frequencies overlapped. The difference between the simulated Q values and the measurement at DESY is shown in Fig. 6.3. It can be seen that there is a certain spread between cavities, but overall the Q values in the real module are slightly higher. In general a good agreement with simulated values can be observed. A larger spread between Q values of different polarisations of the same mode is visible, which can be expected, since manufacturing tolerances, leading to a deviation from a perfect elliptical shape, are responsible for this spread [45].

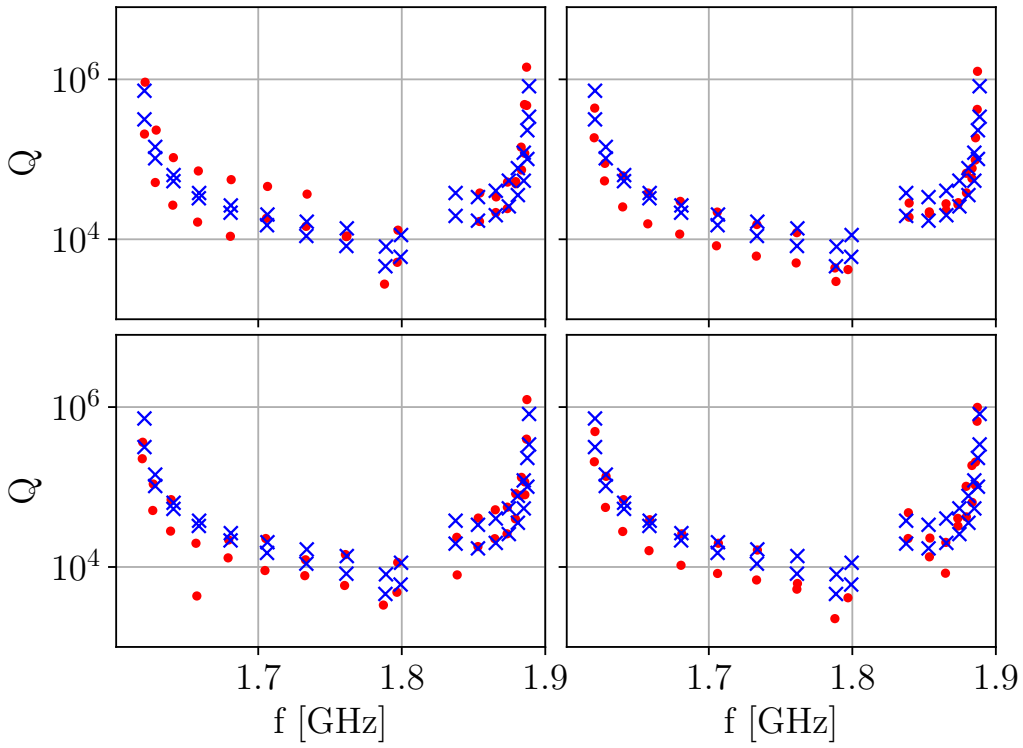

Figure 6.3: Comparison of the simulated Q values (blue) and values measured at DESY (red) of the first two dipole HOM passbands for all four MESA cavities.

6.2 Measurement of the HOM Spectra at HI Mainz

Once the cryomodules were fully assembled and delivered to HI Mainz, an extensive Site Acceptance Test (SAT) was performed. As part of these tests, the HOMs for all four cavities could be measured in the cold 2 K cryostring tuned to the fundamental mode of 1.3 GHz. A short introduction to measurements with a Network Analyzer and possible accuracy limits will be followed by the results of measurements obtained at both cryomodules.

6.2.1 Network Analyzer Basics

A Network Analyzer (NWA) is used for the characterisation of high frequency electrical networks. Network analysis measures the ratios of reflected or transmitted signals to the incident signal. The concept of measuring a transmission line for example, can be understood in a lightwave analogy. Imagine a lens is used as the device under test (DUT). If it is made up of some lossy material, part of the incident wave is absorbed. If it has a reflective surface, some is reflected and most of it will be transmitted. The same is true for transmission line measurements, but the waves are in the RF range instead of the optical range and the DUTs are electrical devices and networks. The concept of scattering parameters (S-parameters) is commonly used to describe the relation between reflected and incident power. The basic principle of a two-port measurement is shown in Fig. 6.4. In the case of a forward transmission measurement, as

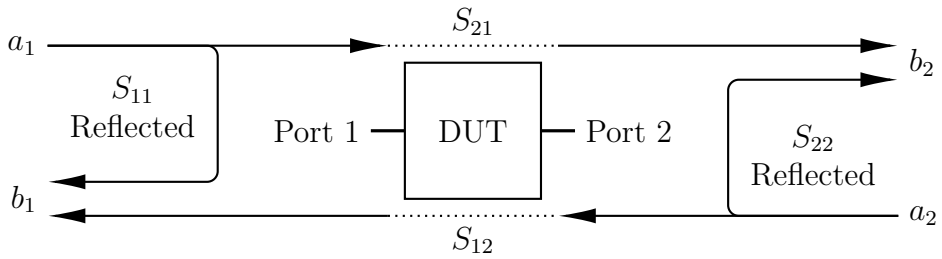

Figure 6.4: Full setup of a two-port S-parameter measurement.

was used to characterize the HOM parameters, the output has to be terminated in a load that matches the characteristic impedance of the test system. This allows to measure the forward reflection coefficient S_{11} (input match) and the forward transmission coefficient S_{21} (gain or loss). The S-parameters are inherently complex, linear quantities however they are often expressed on a logarithmic magnitude scale to reveal more dynamic range. To measure the HOM frequency and quality factor the first port of the NWA is connected to the cavity power coupler via a door knob. The HOM coupler output is then connected to the second port of the NWA in a forward transmission setup. Since each cavity has two HOM coupler, it is possible to measure the signal response either at the long-end HOM coupler or the short-end HOM coupler. The NWA then generates a signal of which the center frequency and span have to be provided by the user. The signal is then swept over the frequency range

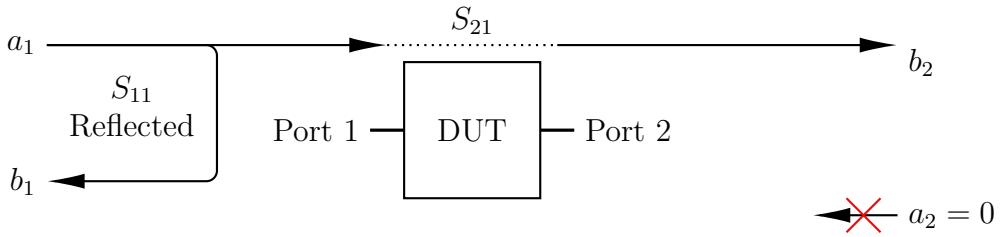

Figure 6.5: Forward transmission setup of a two-port S-parameter measurement. a_2 has been matched to the characteristic impedance of the system.

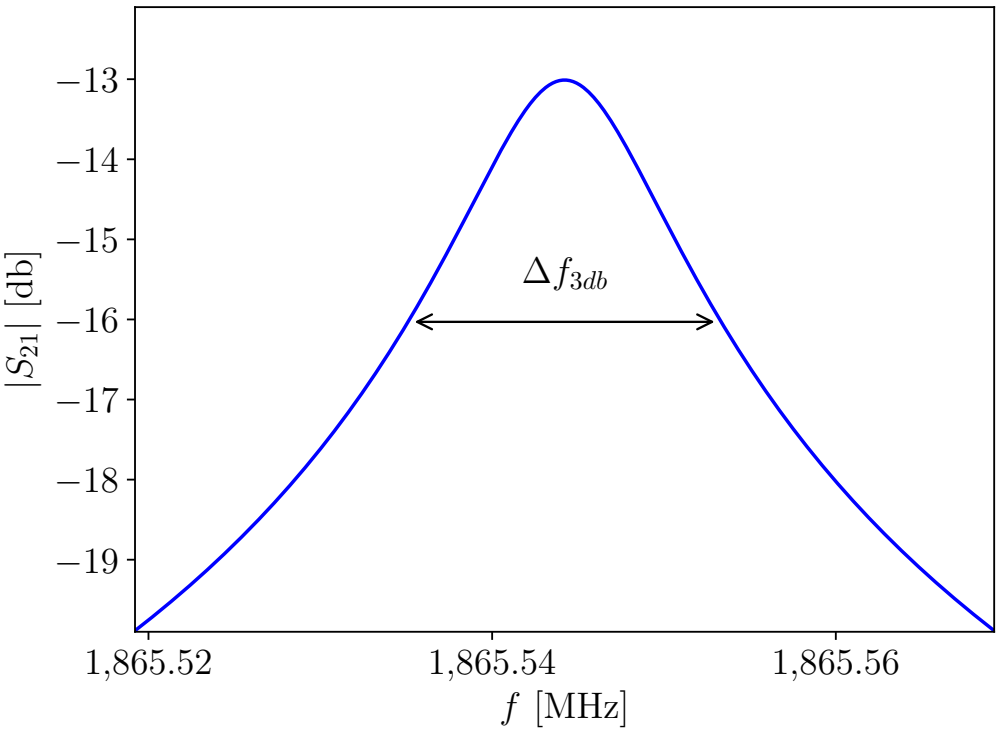

Figure 6.6: Example of a 3 dB measurement. The bandwidth Δf_{3db} is taken at the points where the value of $|S_{21}|$ has dropped to −3 dB of the maximum signal amplitude at the center frequency f_0.

(span) with an intermediate frequency (IF) that can be selected as needed. Smaller IF bandwidths lead to longer measurement time, but better signal to noise ratio. For very narrow frequencies, e.g. HOMs with a high quality factor, a small IF bandwidth of 100 to 300 Hz is used. For smaller quality factors usually IF bandwidths in the order of 1 to 3 kHz are sufficient. Additionally the built in averaging function is used, so that multiple measurements are taken and averaged to further reduce the signal to noise ratio. A 3 dB measurement

is then taken for each single HOM. In Fig 6.6 an idealized situation is shown for explanation. The center frequency f_0 of the HOM is found at the point of maximum magnitude of S_{21}, the bandwidth Δf_{3db} of the HOM is taken at the points, where the value of $|S_{21}|$ has dropped by $-3\,\mathrm{dB}$ of the maximum signal amplitude. The quality factor Q of the HOM is then given by:

$$Q = \frac{f_0}{\Delta f_{3db}} \tag{6.1}$$

6.2.2 Measurement Accuracy Estimation

Typical measurement accuracies achieved for Q value and frequency measurements with a NWA are compared in Ref. [50]. For a low SNR of ≈ 49, as was the worst case for HOM measurements performed at HIM, relative measurement accuracies of 0.015 for the Q values and 1.22×10^{-8} for the center frequency f_0 can be readily achieved. In conclusion the measurement accuracy for HOM parameters is not limited by statistical or device measurement errors but only by systematic uncertainties. For the HOM parameters for example the cool down state of the cryomodule should be equivalent, since temperature dependencies are clearly expected. All measurements taken at HIM were performed over the course of a full week of cold operation of the cryomodule in controlled states. Reproducibility of the data was tested on two different days for the same cavity and values only changed in orders of the NWA measurement accuracy ($\approx 2\,\%$ for the Q values). It would be necessary to measure the HOM parameters again, when the cryomodules are located at their position in the accelerator and cooled down for a longer period of time to check for formerly unnoticed drifts. For the investigation of BBU threshold currents the influence of Q measurement accuracy is neglected.

6.2.3 Resulting HOM Spectra

In total, 18 dipole HOM pairs with two polarisations each were measured for each cavity, making up the first two passbands, including frequencies from 1.6

up to 1.9 GHz. The HOMs are usually separated far enough in frequency to be distinguished from one another without problems, but above 2.4 GHz, where the third passband starts, due to the huge number of quadrupole and even higher-order modes present, dipole modes can no longer be distinguished. In some cases, when the frequencies of two polarisations of the same mode were very close, they could not be distinguished from each other either. The simulation data was then used to identify the mode and polarisation. The frequency spread between all four cavities for each single mode is shown in Fig. 6.7. It is slightly larger than in the case of the undressed cavities as measured at DESY shown in Fig. 6.2.

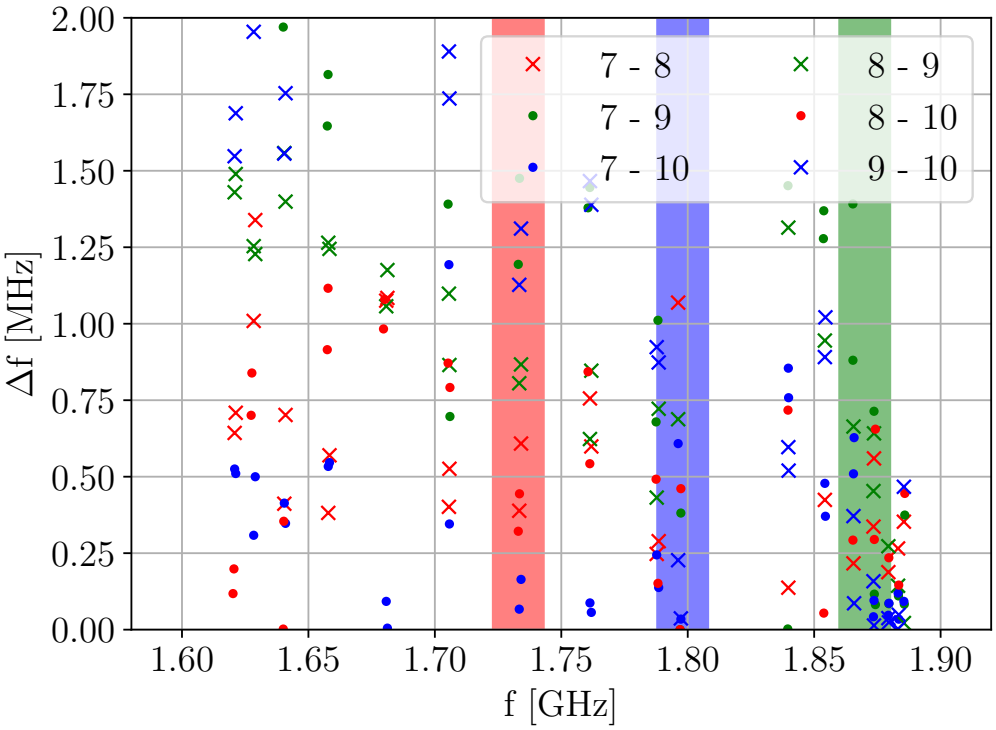

Figure 6.7: Investigation of frequency spread for the data obtained at HIM, where the cavities were mounted into the cryomodule and tuned to 1.3 GHz for the fundamental mode. The maximum observed frequency spread is 1.98 MHz.

This is a result of tuning to the fundamental mode as it is done via changing the shape of the cavity, which fundamentally changes the frequencies of all modes present in that cavity. Since this change in shape is statistically random, an increase in HOM frequency spread could be expected, since there is no

linear correlation between detuning and HOM frequency, at least for multiple HOMs.

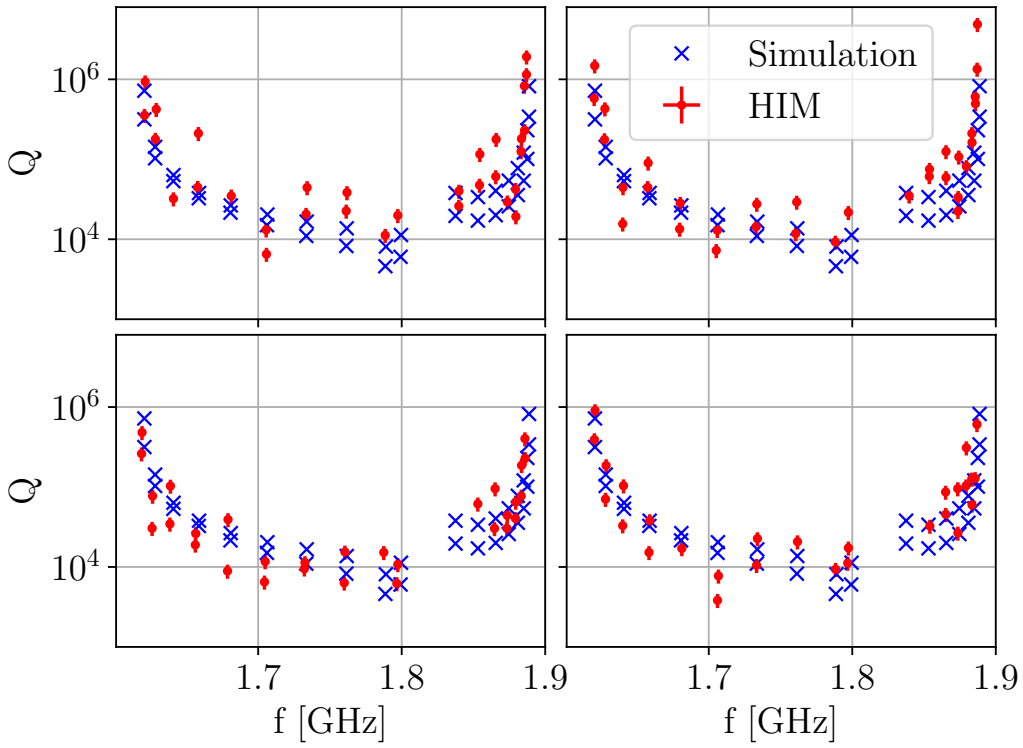

Figure 6.8: Comparison of the simulated Q values (blue) and values measured at HIM (red) for all the 4 cavities numbered 7 to 10 from top left to bottom right. Measurement error is expected to be 2 % and multiplied by a factor of 10 to make it visible.

The difference between the simulated Q values and the measurement at HIM is shown in Fig. 6.8. The results are similar to those presented in Fig. 6.3. The deviations can be explained by results presented in Ref. [45]. In this study, the influence of different deformations of the cavity on the HOM spectra of TESLA cavities were investigated. It turns out that the spread in Q factors is a result of the deformation of the HOM couplers. So the trend of higher Q factors in the measured module can be explained by an increase in the gap width of the capacitive coupling in the HOM coupler. The deviation from the ideal frequency, as it was simulated for the TESLA geometry of the four cavities measured at HIM, is shown in Fig. 6.9. It can be seen that cavity 9 has the largest overall frequency deviation in the first dipole passband and from the bottom left plot in Fig. 6.8 it can be seen that it has also a significant Q factor

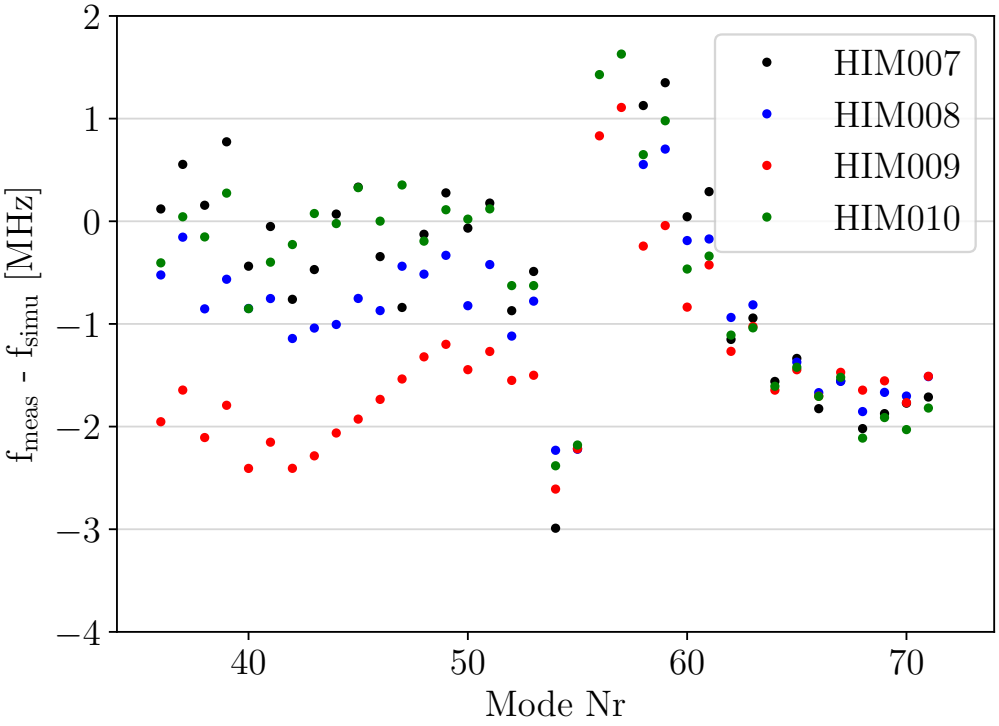

Figure 6.9: Comparison of measured HOM frequencies with the ideal frequencies of the simulation. All four cavities show similar deviations from the ideal case.

spread. The frequency deviation can be understood by a deformation of the iris of the cavity [45]. So cavity 9 is the cavity with the largest deformation of the iris, but still the overall deformation of all the cavities is very small compared to the ones observed in the Tesla Test Facility (TTF) Module 5 measurements. The quality control of the cavity shape was improved after these measurements, resulting in generally smaller deviations of these iris radii of TESLA type cavities produced afterwards. In conclusion of Ref. [45]: "In general, for a dipole pair in the real cavities, its frequencies are shifted to lower values, the mode splitting is larger and the Q_{ext} scattered". It perfectly describes the observed HOM data presented here as well.

6.3 Threshold Current Limit Estimations with bi

The beam instability (bi) code was written by Ivan Bazarov at Cornell [51]. It uses point-like bunches to probe the stability due to HOM deflection by gradually increasing the beam current until instability occurs. Basic tracking information, like energy and position at each cavity, are provided, as well as the transverse beam position for each bunch at the position of the HOM. If the transverse position grows exponentially, instability occurs as shown by the red curve in Fig. 6.10. Below the threshold current, excitation of the HOMs is naturally damped to a point where the deflection due to HOM is negligible as is indicated by the green curve in Fig. 6.10. Additionally, the HOM voltages in

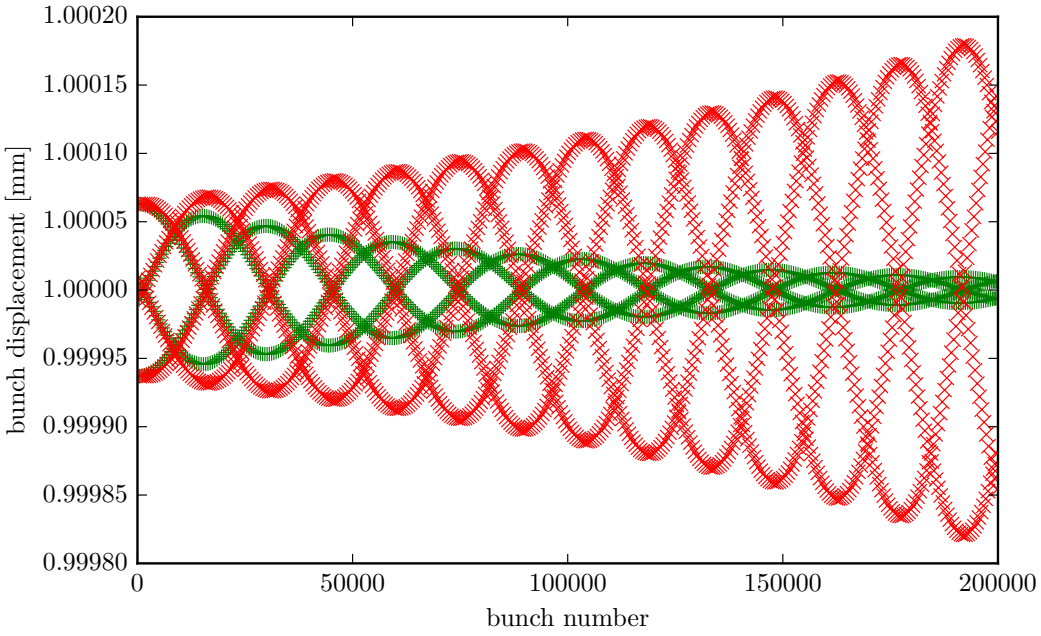

Figure 6.10: Horizontal movement of the beam in the case of HOM excitation. The initial offset of the beam entering the cavity is 1 mm. If an instability occurs, the transverse coordinate will grow exponentially; at the threshold it is constant, and below the threshold the excitation is damped out. The x-axis displays the time scale of the bi simulation represented by the number of bunches passed through a cavity, which can be translated to time with the information on bunch repetition rate being 1.3 GHz in this case.

the transverse planes are collected, which is especially important in the presence of polarized HOMs as it is the case for the TESLA cavities.

6.3.1 Workflow in bi

The bi code requires a parameter file declaring all the beam parameters, including bunch repetition rate, initial probe current, starting energy and many more. It also requires a table with all the HOM parameters present for each cavity. In a first stage, all cavities were filled with the same HOM data from the simulation results; later, each cavity could be assigned their individual HOMs as measured at DESY or HIM respectively. The final and most important part is the 6×6 matrix representation of the MESA lattice as described in section 4.4. After implementing the full ERL lattice in ELEGANT for a start-to-end simulation, it was possible to extract the relevant arc matrices from the tracking results. For the implementation of the cavities with HOMs included, the ELEGANT transfer matrices could not be used, but had to be implemented with the correct cavity edge focussing effects. To allow setting up the HOMs at the individual cavity level, a python wrapper was written to automate most of the lattice construction and to have a top layer to control the bi parameter, lattice and output files. The work flow in bi is visualised in Fig. 6.11.

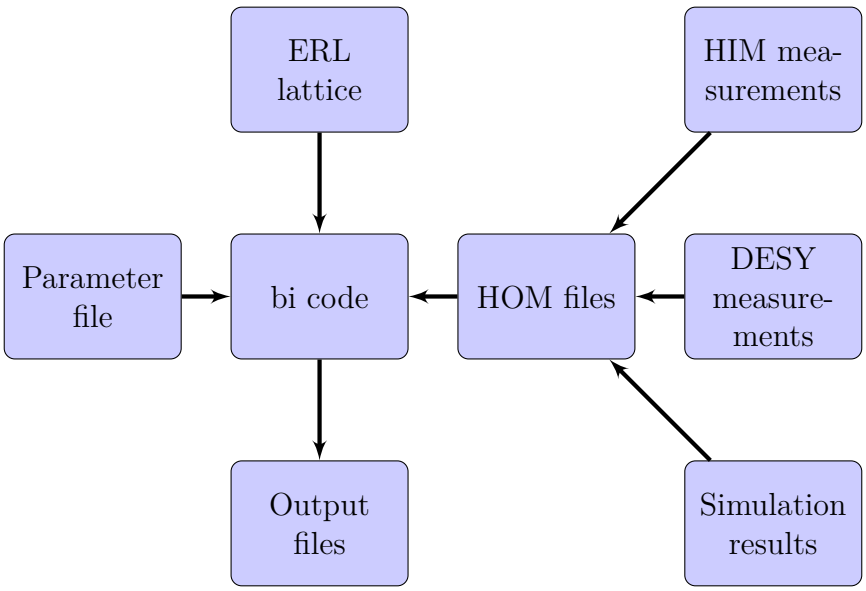

Figure 6.11: Overview of the work flow in bi.

6.3.2 Impact of HOM Frequency Spread

As mentioned earlier, frequency spread between the modes of different cavities is beneficial in increasing the maximum achievable beam current by reducing the crosstalk between cavity HOMs. To test this, a set of 4000 HOM frequencies was generated from a uniform distribution with a spread of 1 MHz. To evaluate the effect of frequency spread, all other parameters were kept constant with $R/Q = 58.604\,\Omega$ and $Q = 20\,000$ for all four cavities for each run. A set of four random frequencies was used for the four cavities and the simulated threshold current result stored. The result of 1000 runs can be seen in Fig. 6.12. For

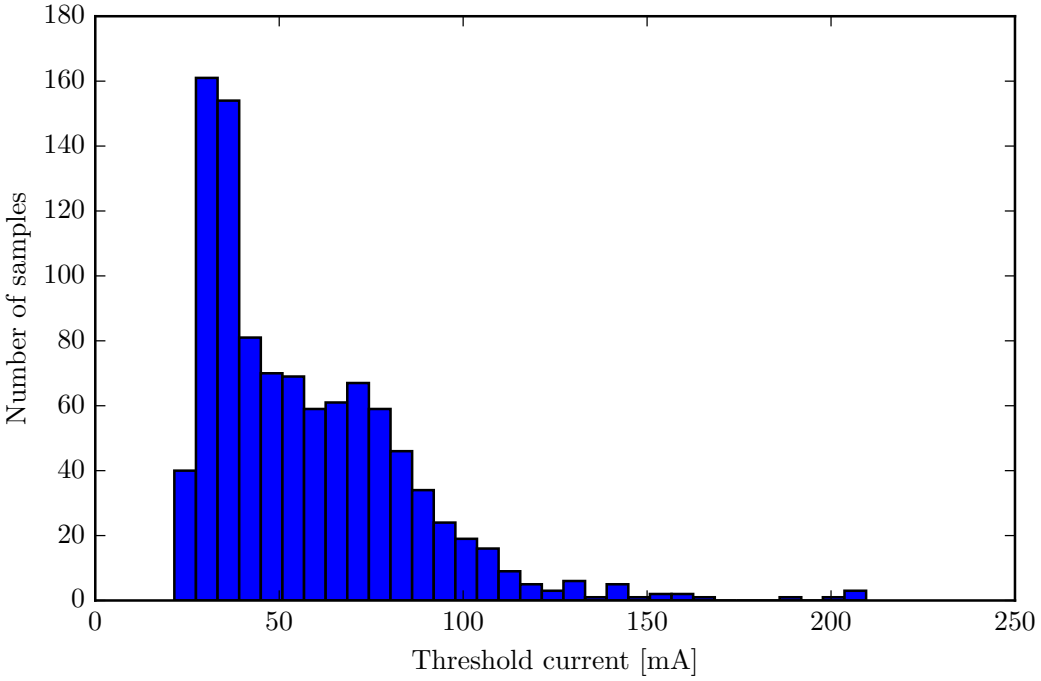

Figure 6.12: Threshold currents for 1000 simulation runs with a frequency spread of 1 MHz.

the case of no frequency spread, the threshold current with these parameters was 14.43 mA; with the inclusion of frequency spread, the minimal threshold current increased to 21.49 mA.

6.4 Threshold Current Limit for the MESA ER Mode

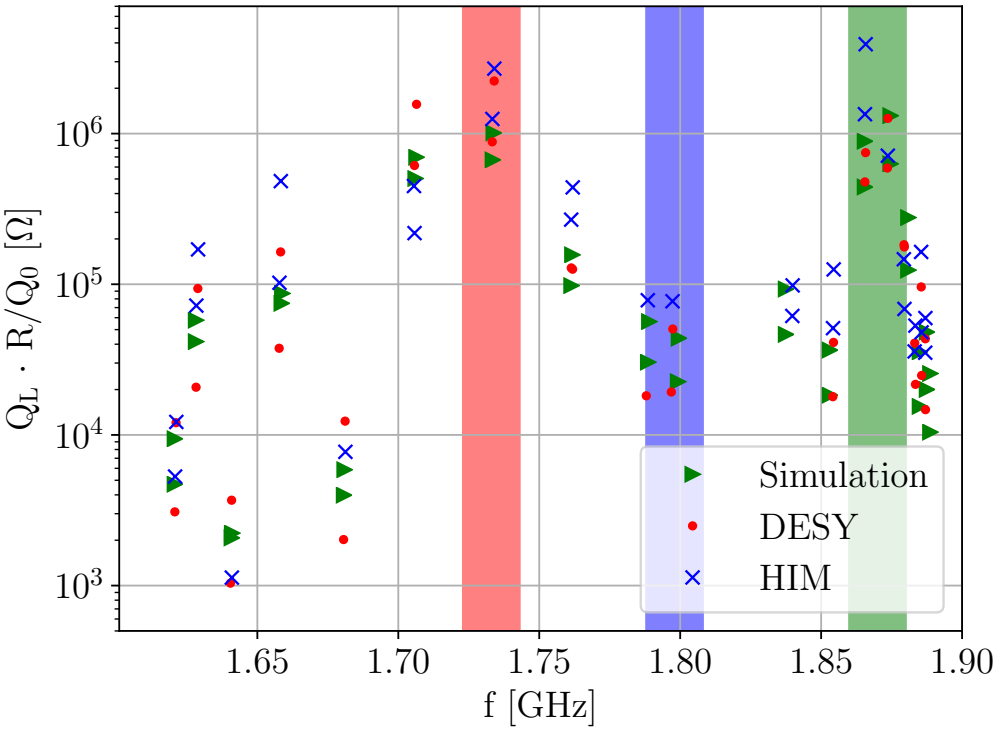

Figure 6.13: Comparison of the Q_L times R/Q_0 values from simulation, as measured in the vertical cryostat at DESY, and with the full module assembled, tuned to the 1.3 GHz fundamental measured at HIM.

For estimation of the threshold current of MESA in ER mode, the lattice starting with the injection arc, including all four individual cavities with their measured or simulated HOMs assigned to them, and the four recirculation arcs are used in simulations with bi. Considering the measured frequency spread presented in Fig. 6.7 and the Q values from Fig. 6.8, three areas of interest can be identified where high $Q_L \cdot R/Q_0$ values marked in Fig. 6.13 coincide with low frequency spread. By assigning both polarisations of each HOM to each cavity and then simulating the threshold current with bi, all 18 pairs of dipole HOMs were scanned and their respective threshold currents simulated [52]. The results of these simulations can be seen in Fig. 6.14. The coloured areas refer to areas where low threshold currents were expected even by just investigating

Eq. 5.16. In the red area, high Q_L values with relatively large R/Q_0 values are present. In the blue area, a relatively low frequency spread compared to the two other areas occurs with smaller R/Q_0 and Q_L values, leading to a much larger threshold current. In the green area, the lowest frequency spread in the measured data is observed, and there are also high Q_L and R/Q_0 values, which leads to the smallest threshold currents at these HOM frequencies. The results

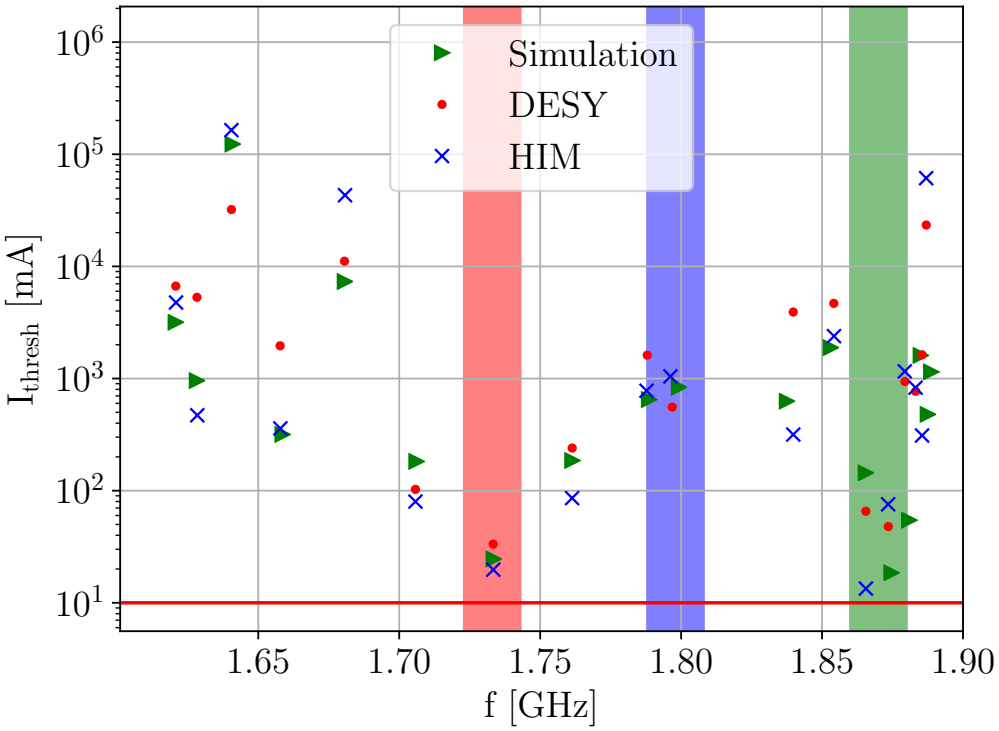

Figure 6.14: Simulation of threshold current values for different data sets. Green: All values from simulated data, red: Q and f values from vertical cold test measurements at DESY, and blue: Q and f values measured in the cryomodule tuned to 1.3 GHz at HIM. The red line denotes the MESA phase-2 10 mA goal.

for the threshold currents given in Fig. 6.14 show that the 10 mA MESA phase-2 current limit could be exceeded in this configuration by all modes that are present in the modules. A maximum threshold current of 13.38 mA is found. Thereby the beam current for MESA is not expected to be limited by BBU at this time, especially not at 1 mA. However, the lowest simulated BBU threshold current lies close to the 10 mA goal for MESA stage 2. Further investigations are needed to enable 10 mA operation in the future.

6.4.1 Multi-turn Threshold Current Scaling

From the approximation formula in section 5.1.2, a scaling of threshold current with the number of recirculations N_r is expected. In Ref. [44], a scaling law for multipass ERLs is derived. In general, one could expect a reduction in achievable threshold current with the number of recirculations squared. From the analytical approximation, a scaling with $N_r(2N_r - 1)$ is expected [44]. To investigate this topic, bi simulations have been performed in a once recirculating configuration accelerating the 5 MeV beam to 55 MeV by passing through both cavities once while accelerating, then passing through both cavities again and decelerating back to 5 MeV. However, a once recirculating machine can also be realised by accelerating twice in both cavities with a final energy of 105 MeV as was suggested for external target experiments where the beam is distorted such that it can't be used for energy recovery. Since the higher-energy beams are more rigid than the low-energy beams, an increase in the achievable beam current is expected for the accelerating configuration compared to the ER mode. These once recirculating results were then compared to the four-pass, twice recirculating ER configuration of MESA. Both the simulated HOM parameters and the measured ones were used for comparison.

HOM data source	accelerating 2-pass	ER 2-pass	ER 4-pass
Simulated HOM data	91.91 mA	83.55 mA	20.65 mA
Measured HOM data	65.60 mA	64.31 mA	13.38 mA

Table 6.1: Comparison for different lattice configurations and two different sets of HOM parameters.

As can be seen from Table 6.1 with only two sets of HOM data and only three possible setups for the MESA lattice, no clear result is obtainable. For the simulated HOM parameters, a clear dependence on N_r^2 is visible between the two-pass ER and the four-pass ER configuration. For the measured HOM parameters, the picture is slightly distorted since more effects than just pure scaling become dominant here. From [44] a scaling of $N_r(2N_r - 1)$ would be expected, which would result in a factor of 6 in threshold current between these two configurations, which is not exactly the case here, but neither is the factor of 4 that would be naively expected.

6.4.2 Quadrupole HOMs

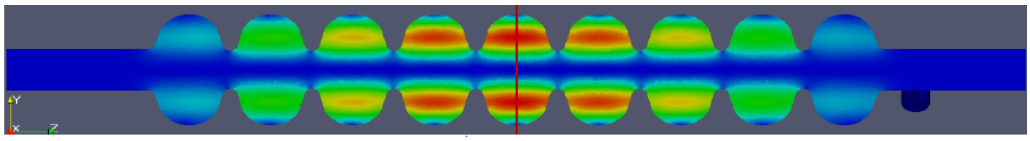

(a) $|\vec{E}|$ of a quadrupole HOM in a TESLA cavity.

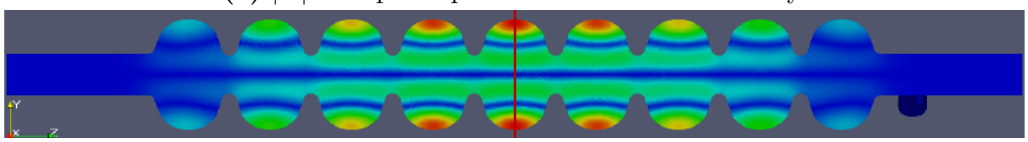

(b) $|\vec{B}|$ of a quadrupole HOM in a TESLA cavity.

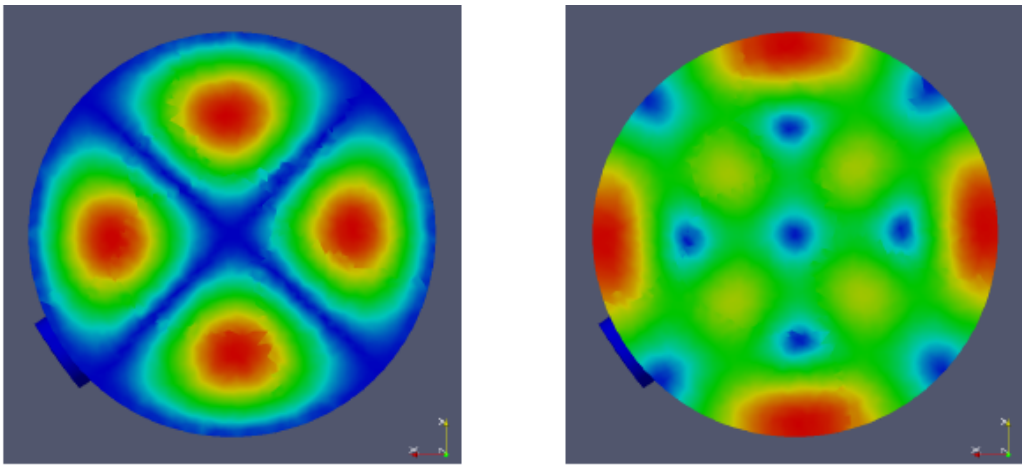

(c) Cut view of $|\vec{E}|$ (left) and $|\vec{B}|$ (right) at the red line indicated in Fig. 6.15a and 6.15b

Figure 6.15: Example of a quadrupole HOM in a TESLA cavity taken from [30] simulated with CST Studio Suite.

The instability mechanism of BBU induced by a quadrupole HOM is different than for dipole HOMs. In Fig. 6.15, an example of a quadrupole HOM inside a TESLA cavity is shown. The energy transfer to quadrupole modes is only zero in the case of a round, on-axis beam; elliptical beams transfer energy to quadrupole modes, which act like a time-dependent quadrupole magnet. If the instability develops, the beam is lost due to over-focussing [53]. An estimate for the threshold current induced by quadrupole HOMs was derived in Ref. [53] and can be estimated as:

$$I_{\mathrm{th,q}} = \frac{2pc^4}{e\omega^3 \left(\frac{R}{Q_0}\right) Q_L(\epsilon_{1x}\beta_{1x}\beta_{2x}\sin(2\mu_x) + \epsilon_{1y}\beta_{1y}\beta_{2y}\sin(2\mu_y))\sin(\omega T)}, \quad (6.2)$$

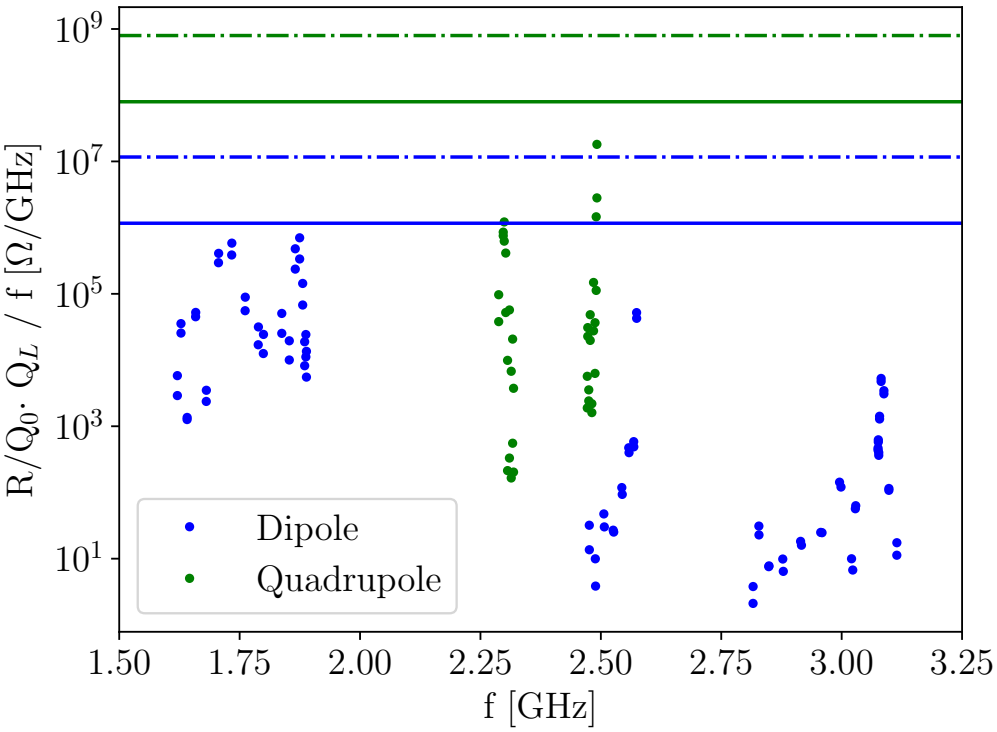

Figure 6.16: Figure of merit for BBU threshold current for all the different dipole (blue) and quadrupole (green) HOMs. The blue (green) line indicates the 10 mA threshold current limited by dipole (quadrupole) HOMs. The dashed lines indicate the 1 mA limit.

for an approximation of the quadrupole HOM limited threshold current, where $\beta_{1x,1y}$ are the initial Twiss beta functions on the first pass, $\beta_{2x,2y}$ are the Twiss beta functions on the second pass, $\mu_{x,y}$ the transverse phase advances and $\epsilon_{x,y}$ the respective emittances. To estimate the influence of quadrupole HOMs, comparing Eq. 6.2 with a simplified version of Eq. 5.16 for a single mode:

$$I_{\mathrm{th,d}} = \frac{2pc^2}{e\omega \left(\frac{R}{Q_0}\right) Q_L(\sqrt{\beta_1\beta_2}\sin(\mu))\sin(\omega T)}, \tag{6.3}$$

reveals that the threshold current for quadrupole HOMs scales as:

$$I_{\mathrm{th,q}} \propto \frac{c^4}{\left(\frac{R}{Q_0}\right) Q_L \omega^3 8\epsilon\beta},$$

if a round beam and equality of all Twiss parameters on first and second pass is assumed. Using the HOM impedance budget $R/Q_0Q_L/f$ as a figure of merit, the quadrupole impedance budget for the same threshold current can be written as:

$$R_q \approx R_d \frac{c^2}{8\omega^2 \epsilon \beta}, \tag{6.4}$$

where R_d is the dipole HOM impedance budget. Assuming typical MESA parameters for the first cavity passed shows that the impedance budget for quadrupole HOMs is approximately a factor of 68 larger at 2.4 GHz. The aforementioned figure of merit for all dipole and quadrupole HOMs is shown in Fig. 6.16. It can be seen that the quadrupole impedance budget, even in this worst case assumption, is still approximately a factor of 5 larger than is necessary for the 10 mA operation. It can be concluded that BBU due to quadrupole HOMs can be neglected for MESA.

6.4.3 Investigation of HOM Polarisation

Let us reconsider Eq. 5.16 and Eq. 5.17:

$$I_{\text{th}} = \frac{-2pc}{e\left(\frac{R}{Q_0}\right)_m Q_{L,m} k_m M^* \sin(\omega_m T_r)},$$

$$M^* = m_{12}\cos^2(\alpha) + (m_{14} + m_{32})\cos(\alpha)\sin(\alpha) + m_{34}\sin^2(\alpha).$$

Depending on the amplitude of the transport matrix elements m_{12}, m_{34} and the polarisation angle α, a clear dependence of the threshold current by HOM polarisation is visible. Since the HOM polarisation itself is very hard to measure in the real cavity, it is interesting to estimate the impact of a slight deviation from the polarisation value predicted by simulations. The threshold current limit is imposed by a mode with a polarisation of $\alpha = 80°$. As can be seen in Fig. 6.17, the trough of the threshold current is at 90°, meaning that the corresponding m_{34} is larger than m_{12} (if viewed in the simple picture of the approximation formula). In the real cavity, polarisation could not be measured, so for all simulation purposes the polarisation values obtained from [30] were used. Considering that the polarisation is a result of the cavities' shape and

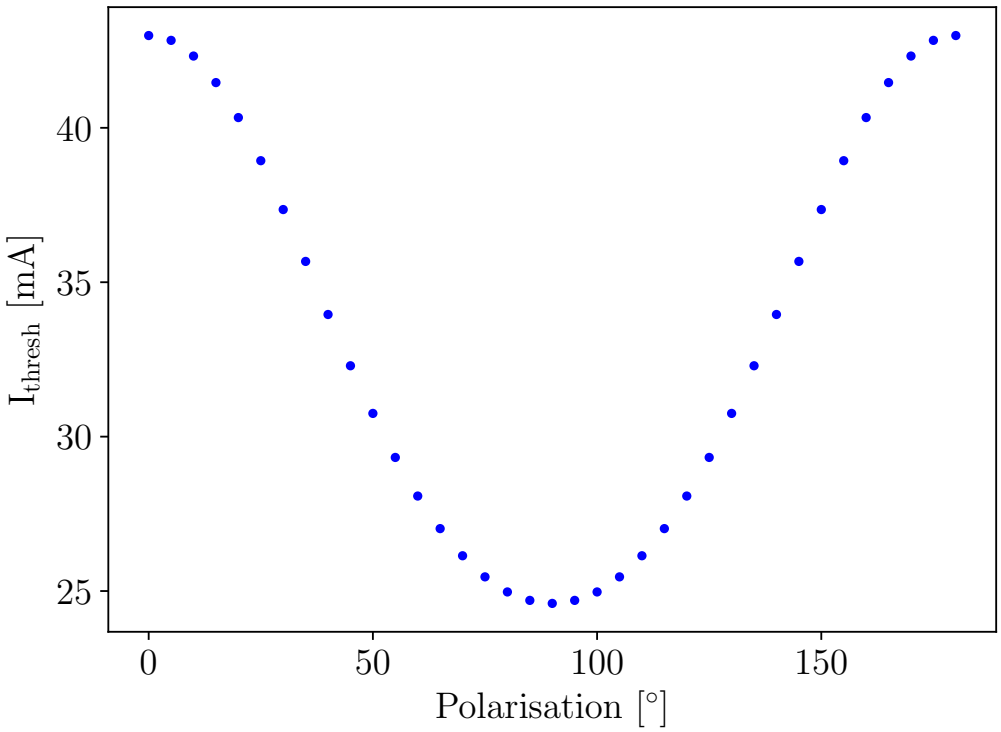

Figure 6.17: Simulation of the threshold current for different polarisation angles of a dipole HOM for the MESA lattice.

geometry, one does not expect its value to change drastically. In Fig. 6.17, it is evident that for the vertical modes at 90° polarisation, small changes only result in higher threshold currents. In the current implementation of the MESA lattice, the threshold current is always limited by the vertical modes, which indicates a high value of m_{34}.

6.4.4 Varying Transverse Phase Advance

During the investigation of HOM polarisation, it was assumed that the m_{ij} matrix elements are constants of the chosen lattice. It is possible to change the phase advance of each transverse dimension individually through readjustments of the quadrupole magnets in the arcs. To simulate the potential of that method, an additional matrix element of length zero was introduced after the first cavity. The method of varying transverse phase advance and its effect on

multi-turn ERLs was described by Lou and Hoffstaetter in Ref. [54]. Following this approach, the additional matrix element reads:

$$M_{\mathrm{pa}}(\phi_x, \phi_y) = \begin{pmatrix} M_x(\phi_x) & \mathbf{0} \\ \mathbf{0} & M_y(\phi_y) \end{pmatrix}, \tag{6.5}$$

where the 2×2 $M_i(\phi_i)$ matrices are given by:

$$M_i(\phi) = \begin{pmatrix} \cos\phi + \alpha_i \sin\phi & \beta_i \sin\phi \\ -\gamma_i \sin\phi & \cos\phi - \alpha_i \sin\phi \end{pmatrix}, \tag{6.6}$$

where $\alpha_i, \beta_i, \gamma_i$ are the Twiss parameters at the position after the cryomodule. This method effectively lowers the M^* matrix element for a certain configura-

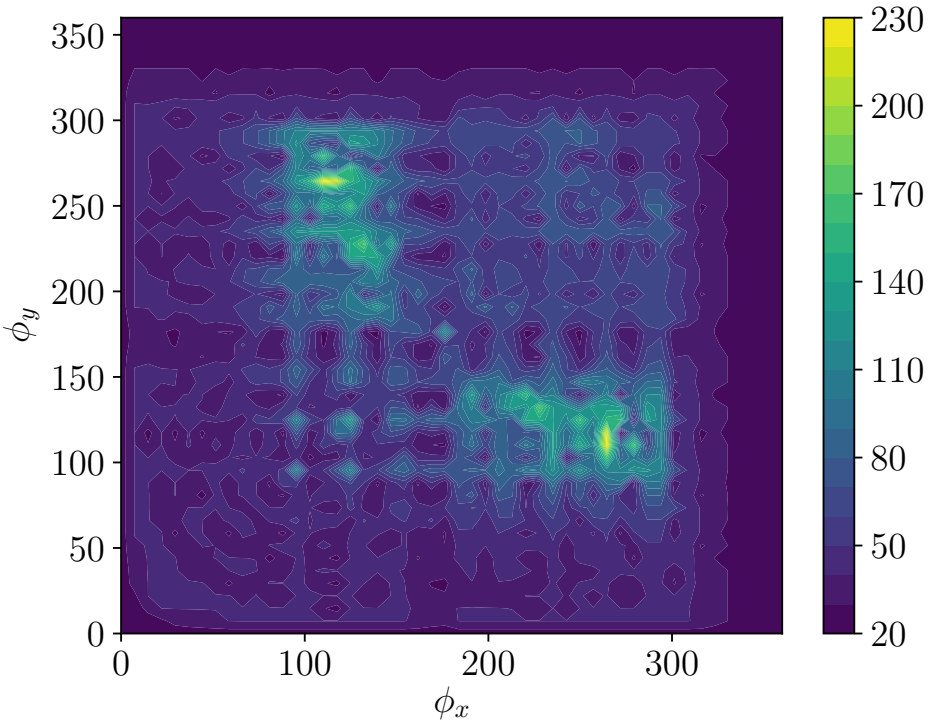

Figure 6.18: Variation of the threshold current as a function of both transverse phase advances. Here, a single pair of dipole HOMs was used and the phase advances varied in steps of 5°. A maximum increase in achievable threshold current by a factor of 10 is possible.

tion, which results in a higher threshold current. For a single HOM, it can be seen directly from the approximation formula that it holds a great potential to

increase the threshold current. To suppress the influence of HOM differences in

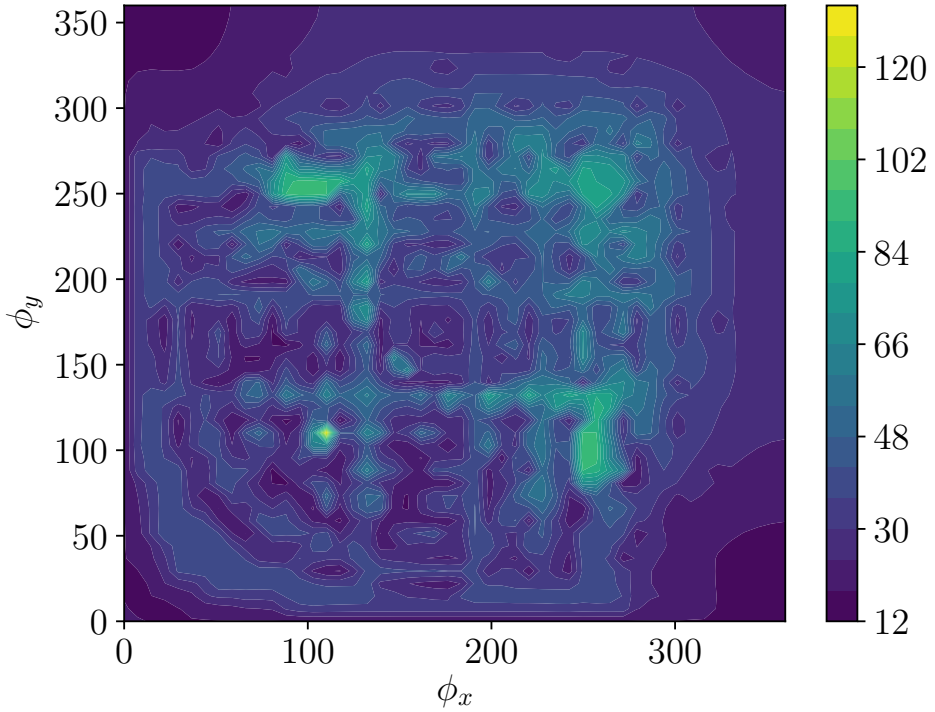

Figure 6.19: Variation of the threshold current as a function of both transverse phase advances. Here, 9 pairs of dipole HOMs were used and the phase advances varied in steps of 10°. A maximum increase in achievable threshold current by a factor of 10 is possible.

the simulation, the HOM parameters were identical for all the cavities in a first investigation. A scan of the transverse phase advances is shown in Fig. 6.18. The color code depicts the threshold current for the different phase advances. A single pair of dipole HOMs was assigned identically to each cavity, which has previously been the one with the lowest threshold current. By varying the phase advance, the threshold current can be increased from 22 mA to about 230 mA. For a single pair of dipole HOMs, it is expected to find a working point with a very high achievable threshold current. It is also interesting to see that there are rather big stable regions with increased currents. It is possible to change the phase advance of the first arc by carefully readjusting the quadrupole magnet strengths in the arc. It seems possible to have a stable beam transport and still be able to increase the threshold current if the necessity arises. Since the cavities contain more than one pair of dipole HOMs, another simulation was

performed with 9 pairs of dipole HOMs. As can be seen in Fig. 6.19, including

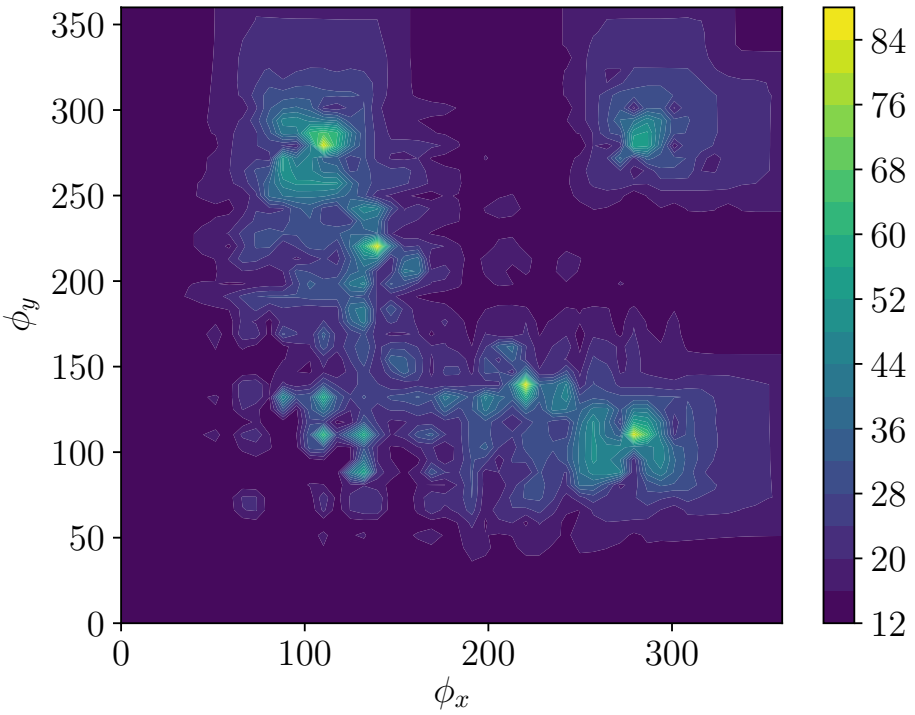

Figure 6.20: Variation of the threshold current as a function of both transverse phase advances. Here, 13 pairs of dipole HOMs from the measurements were used and the phase advances varied. A maximum increase in achievable threshold current by a factor of 7 is possible.

more dipole HOMs decreases the maximum achievable threshold current since there is no longer a single stable configuration. However, in roughly the same region around 110° in both transverse phase advances, a large stable region with a maximum factor of 10 increase in achievable threshold current can be seen. The method of varying transverse phase advances has great potential to increase the achievable threshold current. A final simulation was performed with 13 pairs of HOMs assigned to each cavity, as they were measured at the MESA cavities, including the effects of Q and frequency spread shown in Fig. 6.20. As it can be expected from the mixing of HOM frequencies present in the measured data, higher thresholds are only achievable in certain configurations. It seems possible to find a stable configuration of the arc optics and still increase the BBU threshold by a factor of 2 or even more.

6.5 Beam Current Limits due to HOM Coupler Heating

One potential limit to the maximum beam current for MESA beside the discussed BBU instability results from the heating of the HOM couplers. Even though the HOM couplers were outfitted with sapphire feedthroughs to improve the thermal coupling of the antenna, the niobium tip of the antenna still can quench if too much power is fed to it. This power is not only from HOMs present in the cavity; there is also some residual coupling to the fundamental mode. Even though the coupling to the fundamental mode is minimal, the fundamental mode power fed to the HOM coupler still seems to be the limit in this case. The power that is expected to arrive at each of the HOM antennas from the higher-order modes alone can be extracted from the bi simulation data of the HOM voltages. Simulations of HOM power at the HOM coupler were performed for 1, 5, 10 and 12 mA of beam current for both coupler orientations.

For the 55° orientation of the HOM coupler, a power of 5.7127 mW at 1 mA and 5.7138 mW at 12 mA resulting from HOMs only was calculated. It is safe to assume that HOM coupler heating as a result of HOMs alone would not limit the operation of MESA before BBU occurs above 12 mA, as the power level just grows by some microwatts from 1 mA to 12 mA. To estimate the impact of the coupling of the fundamental mode to the HOM coupler, a formula presented in Ref. [55] can be used to approximate the power stored in the fundamental and other longitudinal modes:

$$P = Nqk_{\parallel}I_{\text{average}}, \tag{6.7}$$

where N is the number of beams in the cavity, q is the bunch charge, $k_{\parallel}$ is the loss factor of the superconducting cavity and I_{average} is the average beam current in the cavity. As can be seen from Table 6.2, for the four MESA beams in ERL mode, a loss factor of $10\,\text{V}\,\text{pC}^{-1}$ and a bunch charge of 7.7 pC at 10 mA result in a rough estimate of 3080 mW for the longitudinal modes stored power. It is expected that some percentage of that power will be absorbed in the HOM

I_{average} [mA]	bunch charge [pC]	longitudinal HOM power [mW]
1	0.77	30.8
5	3.85	770
10	7.7	3080
12	9.24	4435.2

Table 6.2: Approximated longitudinal HOM power for different average currents and bunch charges.

couplers. If we assume 30 % [55], i.e. 1000 mW of the fundamental HOM power to be transferred to the HOM antenna, problems in dissipating this amount of power can be expected. Tests of the 1.5 GHz version of the TESLA HOM coupler for CW operation suggest that with the sapphire feedthrough modification, the critical temperature of niobium will be reached at the antenna tip at a constant power of 43 mW [56]. For investigating these effects of HOM antenna heating operation with high CW beam current is essential. Such experiments require the integration of the module into a working accelerator and could not yet be carried out in the course of this work since MESA is still under construction. It is planned to test a MESA cryomodule with beam in the course of the MESA@bERLinPro project in 2021.

7 Conclusion and Outlook

Assuming a point-like bunch and using the representation of the MESA lattice described in this thesis, a BBU-limited threshold current in the twice recirculating ER mode of 13.4 mA is found. The investigation of the HOM parameters as measured at DESY and HIM shows some differences with the simulations of the TESLA cavity geometry; however these differences are small, expected from simulations of the TESLA geometry, and only detrimental in the case of increased quality factors, while the induced frequency spread, which directly stems from fabrication tolerances, actually improves the achievable threshold current. After being integrated into the cryostat, tuned to the 1.3 GHz fundamental mode and cooled down to 2 K, there was no major difference with the values obtained at DESY before. Together with a start-to-end lattice of MESA, a full picture of the BBU instability induced by dipole HOMs was obtained. Further studies were conducted on the impact of quadrupole HOMs, which was shown to be insignificant for the HOMs that can be expected in the TESLA-type cavities. With the possibility to adjust the betatron phase advances in the first recirculation arc, the threshold current could be significantly increased without having to install additional beam line elements that could further deteriorate the beam. MESA operation in energy recovery mode with 1 mA of beam current is possible and not limited by the beam breakup instability.

It has to be noted, though, that 13.4 mA under perfect conditions is not far above the 10 mA MESA stage-2 goals. Additional work should be done on the influence of machine misalignment, asymmetric bunch distributions and the behaviour of beam halo. Considering off-crest schemes for ERL operation, it would be interesting to investigate multibunch wakefield interaction between

the accelerating and decelerating bunches inside the cavities. The variation of transverse phase advance holds great potential to further increase the threshold current for MESA and should be investigated again for the final layout. A feasibility study should be made with proper arc optics instead of the linear matrix approach. By rematching the first arc of MESA properly, an increase of the threshold current is possible without integrating additional optical elements like skew quadrupoles or sextupoles. Should this method not succeed, there is still the option to include further non-linear optical elements. Currently, another idea to bypass the 13.4 mA beam current limit is to operate a small storage ring in parallel to the MESA accelerator that can be filled in pulsed mode by the MESA ERL. Therein, the beam is brought to interaction with the internal target some 1000 times and then decelerated in the cavities again. With a duty cycle of some percent, that would allow for another upgrade in luminosity for the internal gas target experiments by further increasing the beam current by a factor of 10. Studies for this SI100 project have just begun but further broaden the scientific prospect of MESA. An interesting opportunity to investigate the results presented in this work opens up with the MESA@bERLinPro project [57]. The MESA cryomodule will be available for tests in early 2020, and the bERLinPro project is currently without a main Linac cryomodule for their ERL project. The interesting prospect here is to test the MESA cryomodule in a once recirculating ERL mode with beam currents potentially even higher than 10 mA. It is then possible to investigate the heating of the HOM couplers with beam operation and also try to reach the one-turn BBU threshold current of approximately 65 mA or investigate the HOM coupler signals in pulsed operation and derive the BBU threshold currents from this.

A Appendix

A.1 Example Lattice File and Tracking Code

For illustration purposes, some examples of element definitions in ELEGANT are provided in this section. To define a quadrupole, the length is needed, and the relative strength of the magnetic field is provided by the k1 parameter. A dipole magnet can be implemented as either a sector bend (sbend) or a rectangular magnet (rbend). The length of the orbit through the magnet is provided as well as the bending angle in radians, the magnet gap, and the FINT value, which provides the relative strength of the edge field integral and is assumed to be 0.4 for the dipole magnets used in MESA. For an RF cavity, the length of the cell, the phase reference and the voltage have to be provided. For edge focussing, the Rosenzweig-Serafini model [37] was used with 520 kicks simulated for each cavity.

```
quaddub1: QUADRUPOLE, l = 0.08, k1 = -40.48562189

dridublett: DRIFT, l = 0.05

dip: SBEN, l = 0.3599173516239, angle = 0.78539816339,
 FINT = 0.4, HGAP = 0.025

Linac_I_Cell1: RFCA, l = 0.2563, phase = 46.956, volt =
" 15.813e6 * 0.54 *", N_kicks=520, phase_reference =0,&
  freq = 1.3e9, change_p0 =1, END1_FOCUS = 1, END2_FOCUS = 1,
  BODY_FOCUS_MODEL = SRS
```

By stacking these elements accordingly, combining them in a LINE element, a full element-wise description of the accelerator can be made. With a call of the ELEGANT routine, either tracking can be performed or the evolution of Twiss parameters along the lattice can be computed. The current MESA ER lattice has ≈ 600 elements and lines. A tracking simulation of 50 000 particles through the full lattice takes approximately 5 min using a single CPU core at 4 GHz and 2 GB of RAM. Through a dedicated run file, the output can be controlled, and also input parameters can be provided. For example, the 6×6 matrix of each element can be extracted and used as input for other simulations. The lattice description in MAD-X is very similar to the one in ELEGANT so that scripts are available to translate the basic elements easily from one code to the other.

A.2 List of Publications

BBU simulations for MESA

C. Stoll and F. Hug
J. Phys.: Conf. Ser. 1350 (2019) 012111.
doi:10.1088/1742-6596/1350/1/012111

Incorporation of a MESA Linac module into bERLinPro

B. Kuske, W. Anders, A. Jankowiak, A. Neumann, K. Aulenbacher, F. Hug, T. Stengler and C. P. Stoll
J. Phys.: Conf. Ser. 1350 (2019) 012026.
doi:10.1088/1742-6596/1350/1/012026

Beam matching with space charge in energy recovery Linacs

A. Khan, O. Boine-Frankenheim, F. Hug and C. Stoll
Nuclear Instr. And Meth. A 948 (2019) 162822.
https://doi.org/10.1016/j.nima.2019.162822

Space charge and microbunching studies for the injection arc of MESA

A. Khan, O. Boine-Frankenheim and C. Stoll
J. Phys.: Conf. Ser. 1067 (2018) 062022.
doi :10.1088/1742-6596/1067/6/062022

Beam Breakup Simulations for the MESA Accelerator

C.P. Stoll, F. Hug and D. Simon.
Proc. of the 2017 ERL Workshop, Geneva, Switzerland (2017) 26.
doi:10.18429/JACoWERL2017-MOPSPP009

List of Figures

Bibliography

[1] M. Tigner. A possible apparatus for electron clashing-beam experiments. *Il Nuovo Cimento (1955-1965)*, 37(3):1228–1231, 1965.

[2] H. Merkel. Internal target experiments at the MESA accelerator. *PoS*, page 037, 2016.

[3] G.R. Neil, S. Benson, G. Biallas, C.L. Bohn, D. Douglas, H.F. Dylla, R. Evans, J. Fugitt, J. Gubeli, R. Hill, et al. First operation of an FEL in same-cell energy recovery mode. *Nuclear Instruments and Methods in Physics Research Section A: Accelerators, Spectrometers, Detectors and Associated Equipment*, 445(1-3):192–196, 2000.

[4] F. Hug, K. Aulenbacher, R.G. Heine, B. Ledroit, and D. Simon. MESA - an ERL Project for Particle Physics Experiments. In *Proc. LINAC'16*, number 28 in Linear Accelerator Conference, pages 313–315, Geneva, Switzerland, 5 2017. JACoW. https://doi.org/10.18429/JACoW-LINAC2016-MOP106012.

[5] S. Friederich, K. Aulenbacher, and C. Matejcek. Vacuum lifetime and surface charge limit investigations concerning high intensity spin-polarized photoinjectors. In *Journal of Physics: Conference Series*, volume 1350, page 012045. IOP Publishing, 2019.

[6] C. Matejcek, K. Aulenbacher, and S. Friederich. Low-energy beam transport system for MESA. In *Journal of Physics: Conference Series*, volume 1350, page 012027. IOP Publishing, 2019.

[7] R. Heine, K. Aulenbacher, L. Hein, and C. Matejcek. Current Status of the Milliampere Booster for the Mainz Energy-recovering Superconducting Accelerator. In *Proceedings, 7th International Particle Accelerator Conference (IPAC 2016): Busan, Korea, May 8-13, 2016*, page TUPOW002, 2016.

[8] A. Khan, O. Boine-Frankenheim, and C.P. Stoll. Space charge and microbunching studies for the injection arc of MESA. In *Journal of Physics: Conference Series*, volume 1067, page 062022. IOP Publishing, 2018.

[9] J. Teichert, A. Büchner, H. Büttig, F. Gabriel, P. Michel, K. Möller, U. Lehnert, Ch. Schneider, J. Stephan, and A. Winter. RF status of superconducting module development suitable for CW operation: ELBE cryostats. *Nuclear Instruments and Methods in Physics Research Section A: Accelerators, Spectrometers, Detectors and Associated Equipment*, 557(1):239–242, 2006.

[10] B. Aune. Superconducting TESLA Cavities. *Physical Review Special Topics - Accelerator and Beams*, 3(092001):25, September 2000.

[11] D. Becker, R. Bucoveanu, C. Grzesik, K. Imai, R. Kempf, M. Molitor, A. Tyukin, M. Zimmermann, D. Armstrong, K. Aulenbacher, et al. The P2 experiment. *The European Physical Journal A*, 54(11):208, 2018.

[12] K. Aulenbacher, P.A. Bartolomé, M. Molitor, and V. Tioukine. The MESA polarimetry chain and the status of its double scattering polarimeter. In *AIP Conference Proceedings*, volume 1563, pages 247–250. American Institute of Physics, 2013.

[13] M. Molitor and K. Aulenbacher. A double scattering polarimeter for the P2 experiment at MESA. *PoS*, page 029, 2018.

[14] M. Christmann, P. Achenbach, S. Baunack, P. Burger, A. Denig, L. Doria, F. Maas, and H. Merkel. Instrumentation and optimization studies for a beam dump experiment (BDX) at MESA—DarkMESA. *Nuclear Instruments and Methods in Physics Research Section A: Accelerators, Spectrometers, Detectors and Associated Equipment*, page 162398, 2019.

[15] B. Ledroit and K. Aulenbacher. Collimation of target induced halo following MAGIX at MESA. In *Journal of Physics: Conference Series*, volume 1350, page 012138. IOP Publishing, 2019.

[16] A. Wu Chao and M. Tigner, editors. *Handbook Of Accelerator Physics And Engineering (3rd Printing)*. World Scientific, 1999.

[17] H. Grote and F. Schmidt. MAD-X-an upgrade from MAD8. In *Proceedings of the 2003 Particle Accelerator Conference*, volume 5, pages 3497–3499. IEEE, 2003.

[18] MAD - Methodical Accelerator Design homepage. `https://mad.web.cern.ch/mad/`. Accessed: 2019-10-14.

[19] M. Borland. elegant: A flexible SDDS-compliant code for accelerator simulation. Technical report, Argonne National Lab., IL (US), 2000.

[20] ELEGANT homepage. `https://www.aps.anl.gov/Accelerator-Operations-Physics/Software`. Accessed: 2019-10-14.

[21] F. Hug and R.G. Heine. Injector linac stability requirements for high precision experiments at MESA. *Journal of Physics: Conference Series*, 874:012012, jul 2017.

[22] A. Khan, O. Boine-Frankenheim, F. Hug, and C.P. Stoll. Beam matching with space charge in energy recovery linacs. *Nuclear Instruments and Methods in Physics Research Section A: Accelerators, Spectrometers, Detectors and Associated Equipment*, 948:162822, 2019.

[23] D. Reschke. Performance of Superconducting Cavities for the European XFEL. In *Proceedings, 7th International Particle Accelerator Conference (IPAC 2016): Busan, Korea, May 8-13, 2016*, page THYB01, 2016.

[24] T. Peterson, T. Arkan, C. Ginsburg, Y. He, J. Kaluzny, M. McGee, and Y. Orlov. LCLS-II 1.3 GHz Cryomodule Design - Modified TESLA-Style Cryomodule for CW Operation. In *Proceedings, 17th International Conference on RF Superconductivity (SRF2015): Whistler, Canada, September 13-18, 2015*, page THPB119, 2015.

[25] A. Jankowiak. The Mainz Microtron MAMI–Past and future. *The European Physical Journal A-Hadrons and Nuclei*, 28(1):149–160, 2006.

[26] F. Hug, K. Aulenbacher, T. Kürzeder, E. Schilling, D. Simon, A. Skora, T. Stengler, and S. Thomas. Cryogenic Installations for Module Tests at Mainz. In *19th Int. Conf. on RF Superconductivity (SRF'19), Dresden, Germany, 30 June-05 July 2019*, pages 997–1002. JACOW Publishing, Geneva, Switzerland, 2019.

[27] O. Shevchenko, V. Arbuzov, K. Chernov, I. Davidyuk, E. Dementyev, B. Dovzhenko, Ya Getmanov, B. Knyazev, E. Kolobanov, A. Kondakov, V. Kozak, E. Kozyrev, V.V. Kubarev, G. Kulipanov, E. Kuper, I. Kuptsov, G. Kurkin, S. Motygin, V. Osipov, and P. Vobly. Current status of the novosibirsk infrared FEL and the third stage lasing. *Physics of Particles and Nuclei Letters*, 13:1002–1005, 12 2016.

[28] K. Wille. *Physik der Teilchenbeschleuniger und Synchrotronstrahlungsquellen: Eine Einführung.* Springer-Verlag, 1996.

[29] P. Heil. Longitudinale Emittanzanpassung durch Geschwindigkeitsmodulation im Injektionssystem an MESA. Master's thesis, 2015.

[30] W. Ackermann, H. De Gersem, C. Liu, and T. Weiland. Eigenmode Calculations for the TESLA Cavity Considering Wave-Propagation Losses through Fundamental and Higher-Order Mode Couplers. page 227, 2015.

[31] J. Andruszkow, A. Liero, H. Timm, K. Rothemund, P. Zhogolev, M. Serio, V. Gorbunov, E. Merker, U. Zobjack, Y. Cho, et al. TESLA: The superconducting electron positron linear collider with an integrated X-ray laser laboratory. Technical design report. Pt. 2: The accelerator. Technical report, 2001.

[32] M. Altarelli, R. Brinkmann, M. Chergui, W. Decking, B. Dobson, S. Düsterer, G. Grübel, W. Graeff, H. Graafsma, J. Hajdu, et al. The european x-ray free-electron laser technical design report. *DESY*, 97(2006):4, 2006.

[33] P. Michel, H. Buettig, F. Gabriel, M. Helm, U. Lehnert, Ch. Schneider, R. Schurig, W. Seidel, D. Stehr, J. Teichert, et al. The rossendorf ir-fel elbe. In *Proc. FEL*, page 488. Citeseer, 2006.

[34] W. Singer, A. Brinkmann, R. Brinkmann, J. Iversen, A. Matheisen, W.D. Moeller, A. Navitski, D. Reschke, J. Schaffran, A. Sulimov, et al. Production of superconducting 1.3-GHz cavities for the European X-ray Free Electron Laser. *Physical Review Accelerators and Beams*, 19(9):092001, 2016.

[35] T. Stengler. *Entwicklung eines supraleitenden Beschleunigermoduls für den rezirkulierenden Betrieb am Mainz Energy-Recovering Superconducting Accelerator (MESA).* PhD thesis, Johannes Gutenberg-Universität Mainz, 2020.

[36] T. Stengler, K. Aulenbacher, F. Hug, and S. Thomas. SRF testing for Mainz Energy Recovering Superconducting Accelerator MESA. In *19th Int. Conf. on RF Superconductivity (SRF'19), Dresden, Germany, 30 June-05 July 2019*, pages 508–512. JACOW Publishing, Geneva, Switzerland, 2019.

[37] J. Rosenzweig and L. Serafini. Transverse particle motion in radio-frequency linear accelerators. *Physical Review E*, 49(2):1599, 1994.

[38] F. Hug. Application of Non-Isochronous Beam Dynamics in ERLs for Improving Energy Spread and Beam Stability. In *Proceedings, 8th International Particle Accelerator Conference (IPAC 2017): Copenhagen, Denmark, May 14-19, 2017*, page MOPVA013, 2017.

[39] W. K. H. Panofsky and R. B. Neal. Electrons Accelerated to 10-20 GeV Range. *SLAC-Pub-197*, 1966.

[40] R. H. Helm, H. A. Hogg, R. F. Kootz, G. A. Loew, R. H. Miller, and R. B. Neal. Recent Beam Performance and Developments at SLAC. *IEEE Transactions on Nuclear Science*, 16(3):311–5.

[41] F. Lin. Storage-ring Electron Cooler for Relativistic Ion Beams. In *Proceedings, 7th International Particle Accelerator Conference (IPAC 2016): Busan, Korea, May 8-13, 2016*, pages 2466–2468, 2016.

[42] E. Pozdeyev. Regenerative multipass beam breakup in two dimensions. *Phys. Rev. ST Accel. Beams*, 8:054401, May 2005.

[43] H. Padamsee, J. Knobloch, T. Hays, et al. *RF superconductivity for accelerators*, volume 2011. Wiley Online Library, 2008.

[44] G.H. Hoffstaetter and I.V. Bazarov. Beam-breakup instability theory for energy recovery linacs. *Physical Review Special Topics - Accelerator and Beams*, 7(054401):13, May 2004.

[45] L. Xiao, C. Adolphsen, V. Akcelik, A. Kabel, K. Ko, L. Lee, Z. Li, and C. Ng. Modeling imperfection effects on dipole modes in TESLA cavity. In *2007 IEEE Particle Accelerator Conference (PAC)*, pages 2454–2456, June 2007.

[46] W. Lou and G.H. Hoffstaetter. Beam-breakup studies for the 4-pass Cornell-Brookhaven Energy-recovery test accelerator. *Journal of Physics: Conf. Series 1067(2018) 062014*, 2018.

[47] C.P. Stoll, F. Hug, and D. Simon. Beam Break Up Simulations for the MESA Accelerator. In *Proc. 59th ICFA Advanced Beam Dynamics Workshop (ERL'17), Geneva, Switzerland, June 18-23, 2017*, number 59 in ICFA Advanced Beam Dynamics Workshop, pages 26–28, Geneva, Switzerland, May 2018. JACoW Publishing. https://doi.org/10.18429/JACoW-ERL2017-MOPSPP009.

[48] D.R. Douglas, K.C. Jordan, L. Merminga, E.G. Pozdeyev, C.D. Tennant, H. Wang, T.I. Smith, S. Simrock, I.V. Bazarov, and G.H. Hoffstaetter. Experimental investigation of multibunch, multipass beam breakup in the Jefferson Laboratory Free Electron Laser Upgrade Driver. *Phys. Rev. ST Accel. Beams*, 9:064403, Jun 2006.

[49] T. Stengler. Cryotests at DESY Hamburg.

[50] P.J. Petersan and S.M. Anlage. Measurement of resonant frequency and quality factor of microwave resonators: Comparison of methods. *Journal of applied physics*, 84(6):3392–3402, 1998.

[51] I.V. Bazarov. bi - beam instability BBU code. http://www.lepp.cornell.edu/ ib38/bbucode/src.

[52] C.P. Stoll and F. Hug. Beam breakup simulations for the Mainz Energy recovering Superconducting Accelerator MESA. *Journal of Physics: Conference Series*, 1350:012111, Nov 2019.

[53] Y. Petenev. *Analysis of injection and recovery schemes for ERL based light source.* PhD thesis, 2014.

[54] W. Lou and G.H. Hoffstaetter. Beam break-up current limit in multi-turn ERLs and CBETA, 2018.

[55] L. Merminga, D.R. Douglas, and G.A. Krafft. High-current energy-recovering electron Linacs. *Annual Review of Nuclear and Particle Science*, 53(1):387–429, 2003.

[56] J. Sekutowicz. HOM Damping and Power Extraction from superconducting Cavities. In *Proceedings of LINAC 2006, Knoxville, Tennessee USA*, 2006.

[57] B. Kuske, W. Anders, A. Jankowiak, A. Neumann, K. Aulenbacher, F. Hug, T. Stengler, and C. P. Stoll. Incorporation of a MESA linac module into bERLinPro. *Journal of Physics: Conference Series*, 1350:012026, Nov 2019.